ORIGINAL PAPER

Paul König · Patrick Salcher · Christoph Adam ⬤ · Benjamin
Hirzinger

Dynamic analysis of railway bridges exposed to high-speed trains considering the vehicle–track–bridge–soil interaction

Abstract A new semi-analytical approach to analyze the dynamic response of railway bridges subjected to high-speed trains is presented. The bridge is modeled as an Euler–Bernoulli beam on viscoelastic supports that account for the flexibility and damping of the underlying soil. The track is represented by an Euler–Bernoulli beam on viscoelastic bedding. Complex modal expansion of the bridge and track models is performed considering non-classical damping, and coupling of the two subsystems is achieved by component mode synthesis (CMS). The resulting system of equations is coupled with a moving mass–spring–damper (MSD) system of the passing train using a discrete substructuring technique (DST). To validate the presented modeling approach, its results are compared with those of a finite element model. In an application, the influence of the soil–structure interaction, the track subsystem, and geometric imperfections due to track irregularities on the dynamic response of an example bridge is demonstrated.

1 Introduction

In the last two decades, the importance of the dynamics of railway bridges has grown considerably due to the increased development of high-speed railway lines. In fact, at high, so-called critical train speeds, resonance phenomena occur more frequently in bridge structures, resulting from excitation by the moving axle loads at constant spacing, as well as from track irregularities and wheel hunting movements. Resonance phenomena in railway bridges usually do not lead to a loss of load-bearing capacity, but to the exceeding of the maximum allowable accelerations of the bridge deck. In such cases, the ballast bed becomes instable, reducing the maintenance intervals for the track or requiring a reduction in train speed. In catastrophic conditions, the change in track position may even lead to train derailments. The numerical prediction of the dynamic response of railway bridges is therefore of great importance.

First studies on the dynamic behavior of railway bridges date back to the nineteenth century (e.g., [32,38]), as described in the comprehensive overview of early contributions in [16]. The simplest approaches dealing

P. König · P. Salcher · C. Adam (✉) · B. Hirzinger
Unit of Applied Mechanics, University of Innsbruck, Technikerstr. 13, 6020 Innsbruck, Austria
E-mail: christoph.adam@uibk.ac.at

P. König
E-mail: paul.koenig@uibk.ac.at

P. Salcher
E-mail: patrick.salcher@uibk.ac.at

B. Hirzinger
VCE Vienna Consulting Engineers ZT GmbH, Untere Viaduktgasse 2, Vienna, Austria
E-mail: hirzinger@vce.at

with these problems include the modeling of the bridge as a beam-like structure subjected to moving single loads, which correspond to the axle loads of the train [13,17,36]. In more complex models, the bridge is represented by a 3D finite element (FE) model and the train as a 3D mass–spring–damper (MSD) system [40] in which rigid bodies are connected by lumped spring–damper elements [31,46]. To determine the dynamic response of the coupled system, in a classical approach, both subsystems are first treated individually and then coupled via a coupling condition at the point of contact [45]. However, these models can only be created with great effort and do not allow parameter studies or stochastic simulations. The simplest model approach to explicitly consider the dynamic interaction between train and bridge consists of a beam for the bridge and a plane MSD system for the train [41,44]. These, as well as other simplifying models (e.g., [10] and [22]), are suitable for computationally intensive investigations of the failure probability of railway bridges using stochastic simulations [21]. In these simplified beam models, the track is not explicitly modeled. An exception is the model presented in [3], where the track is represented as an additional beam, which rests on viscoelastic bedding on the bridge and the adjacent areas to be connected. For the coupling of the subsystems of the bridge beam and track beam, the authors of [3] used a variant of the so-called component mode synthesis (CMS).

A recent contribution on vehicle–bridge interaction [33] proposed a method to decouple the vehicle–bridge interaction problem, taking the influence of the traversing vehicle on the natural frequencies and damping of the bridge [34] into account. Other recent studies have shown that the soil–structure interaction can have a significant impact on the prediction of the dynamic bridge response [5,35,37,42]. Discretization of the half-space and foundations by means of finite elements or boundary elements [18,30,37] leads to a computational effort that is hardly feasible. Alternatively, the soil can be represented in a simplified manner by spring–damper elements below the bridge supports [11,39]. In a recent paper [20], such a beam model on viscoelastic supports crossed by a moving MSD system was developed. The solution of this coupled non-classically damped system was found by means of a dynamic substructuring technique (DST), and the approach of the MSD system at the beam and its departure after crossing the beam were approximated by simplifying assumptions.

The aim of the present contribution is to extend this non-classically damped model of the bridge beam [20] by a track on viscoelastic bedding. The CMS approach for simply supported single-span beams presented in [3] serves as a basis for considering the track substructure as a separate beam. The proposed model is thus able to capture the load distribution by the track on the bridge structure. Consequently, there is no need for simplified assumptions for the approach and departure conditions of the train, as described in [20]. In addition, track irregularities are accounted for by appropriate irregularity profile functions [8]. This way, the proposed model captures the dynamic train–track–bridge–soil interaction including track irregularities and provides a solid basis for further numerical investigations.

In the present paper, first the models and the corresponding equations of motion of the individual subsystems, track, bridge–soil, and train, are described. A modal expansion of the soil–bridge and track subsystems is performed, and the coupling of the subsystem is achieved using CMS [2,3]. This set of equations is then coupled with the MSD system of the train using a DST and subsequently solved numerically. In order to validate the proposed model, a numerical study is carried out comparing the results of the presented method with those of a finite element model. Further numerical investigations include the comparison of the response with and without track substructure and the results with and without soil–structure interaction, with aspects of each subsystem discussed. Finally, some important findings on the consideration of rail irregularities are presented.

2 Modeling of the train–track–bridge–soil system

For the present investigations, the interaction system consisting of the high-speed train moving at constant speed v, the track, the bridge with foundation, and the soil is modeled as a plane system, which is shown in Fig. 1. The rails and the slender bridge are both modeled as Euler–Bernoulli beams with constant cross-section. The rail system on top of the bridge is resting on a viscoelastic Winkler bedding, which represents the mechanical properties of the track and the underlying subgrade. Rail irregularities are taken into account by introducing random irregularity profile functions on the rail beam surface [8], which describe the deviation from a perfectly smooth track. The viscoelastic bearings at both ends of the bridge beam represent the stiffness and damping of the supporting soil. To account for the mass of the foundation and the soil above the foundation, lumped masses at each end of the bridge are added. It is assumed that a conventional train composed of N_c individual vehicles crosses the bridge. Each vehicle, which consists of a car body, two bogies, and four axles, is modeled as a mass–spring–damper (MSD) system with ten degrees of freedom (DOFs).
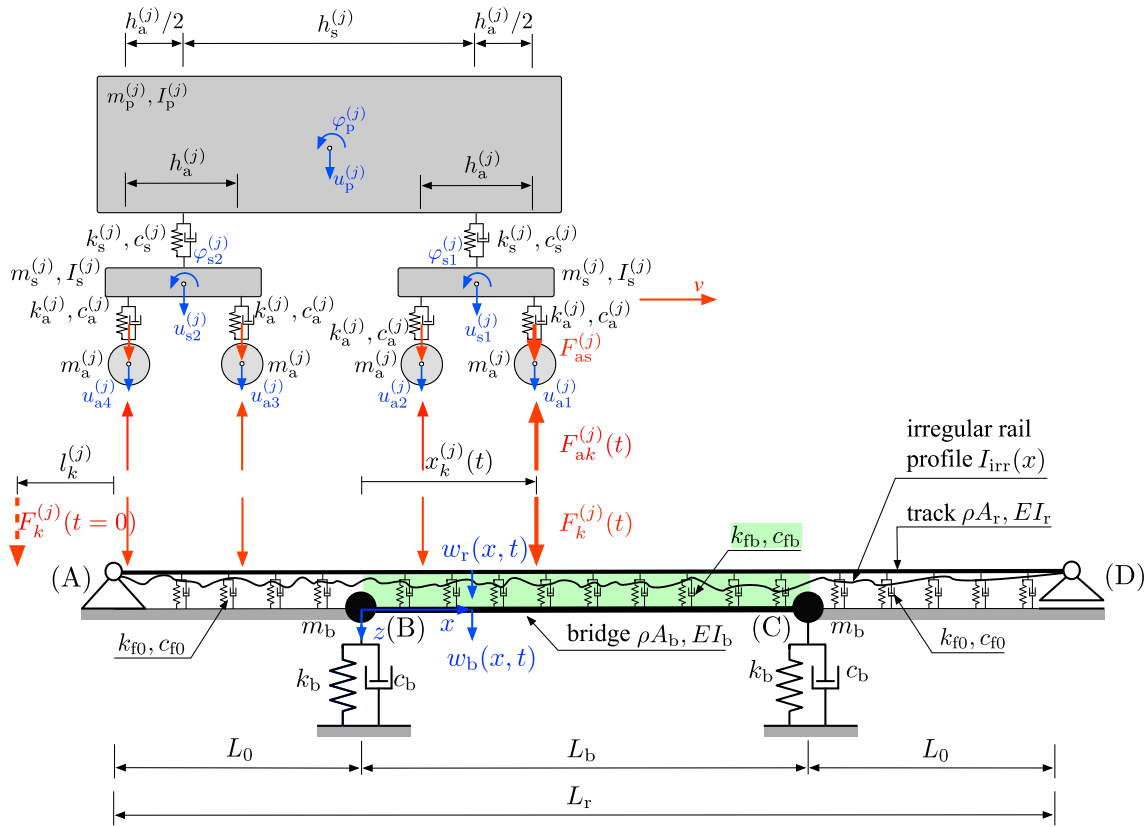
Fig. 1 Viscoelastically supported single-span bridge model with track crossed by a planar MSD model, which represents the jth train vehicle

3 Equations of motion and boundary conditions

The interacting system shown in Fig. 1 is at first split into the subsystems of the track, the bridge–soil, and the train. In this Section, the equations of motions of each subsystem are presented.

3.1 Track subsystem

The Euler–Bernoulli beam with the length L_r, which represents the track substructure, has a constant mass per unit length ρA_r and a constant flexural rigidity EI_r and rests on a viscoelastic Winkler bedding with stiffness coefficient $k_f(x)$ and damping coefficient $c_f(x)$. The bedding parameters can be different in the bridge section (then denoted as k_{fb} and c_{fb}) and in the area of the subsoil (then denoted as k_{f0} and c_{f0}). The origin of the axial coordinate $x = 0$ is located at the left viscoelastic bridge bearing. In the model, the theoretically infinitely long track superstructure is considered to be simply supported at both ends. To ensure that the effects of these "artificially" introduced boundary conditions on the system response at the bridge are negligible, the track in the model must have the following minimum length before and after the bridge [3,12]:

$$L_0 \geq 2\pi \sqrt[4]{\frac{4EI_r}{k_{f0}}}. \tag{1}$$

The deflection $w_r(x, t)$ of the track model is governed by the following equation of motion [9]:

$$\rho A_r \ddot{w}_r(x, t) + EI_r w_{r,xxxx}(x, t) = -q_r(x, t) + f_r(x, t). \tag{2}$$

The distributed force $q_r(x, t)$ results from the viscoelastic bedding counteracting the displacement of the track,

$$
\begin{aligned}
q_r(x, t) =& k_f(x)\left(w_r(x, t) - w_b(x, t)\Pi(x, 0, L_b)\right) \\
& + c_f(x)\left(\dot{w}_r(x, t) - \dot{w}_b(x, t)\Pi(x, 0, L_b)\right),
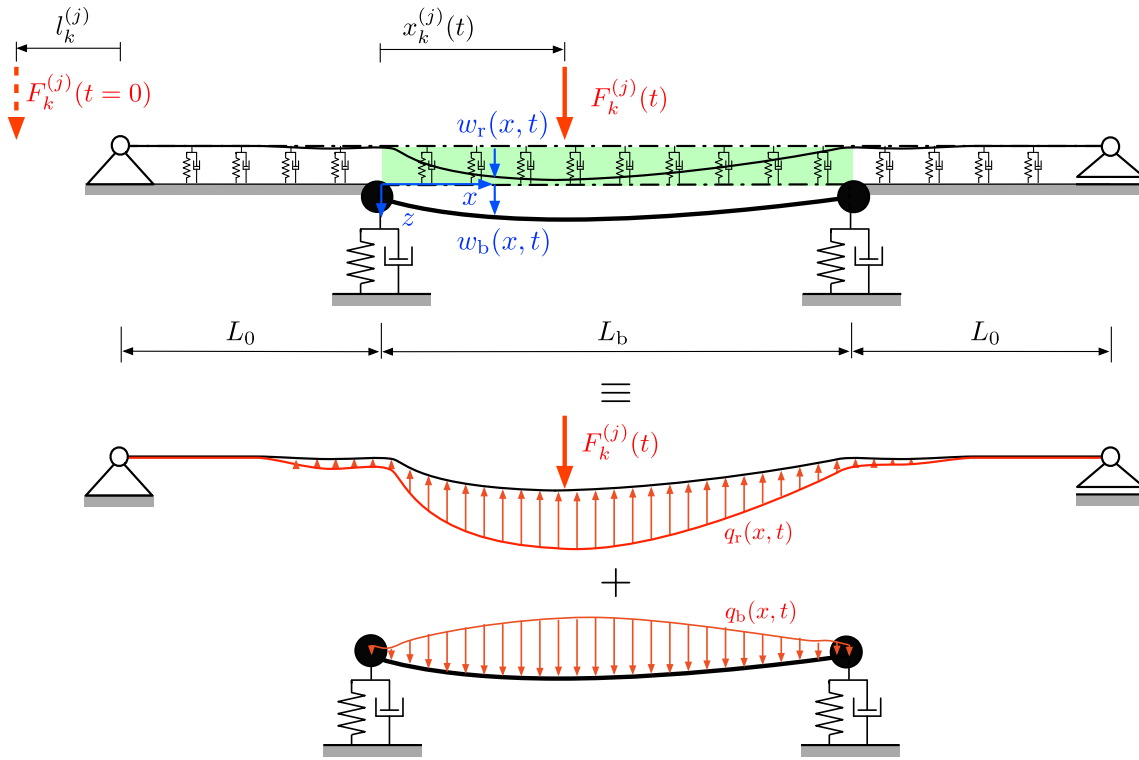\end{aligned}
\tag{3}
$$

Fig. 2 Track–bridge–soil subsystem subjected to one moving interaction load and free-body diagram separating the track and the bridge–soil subsystems

where w_b denotes the vertical displacement of the beam representing the bridge substructure of length L_b, as shown in Fig. 2. The window function $\Pi(x, 0, L_b) = H(x) - H(x - L_b)$ composed of the Heaviside step functions $H(x)$ and $H(x - L_b)$ delimits the range of the viscoelastic bedding on top of the bridge beam from the remaining track beam area. It thus indicates that the bridge deflection $w_b(x, t)$ has an effect on the force $q_r(x, t)$ only over the bridge span L_b.

The second part of the forcing function in Eq. (2), $f_r(x, t)$, captures the effect of the interaction forces between the rails and the vehicles,

$$f_r(x, t) = \sum_{j=1}^{N_c} \sum_{k=1}^{n_a^{(j)}} F_k^{(j)}(t) \delta\left(x - x_k^{(j)}(t)\right) \Pi\left(t, t_{Ak}^{(j)}, t_{Dk}^{(j)}\right). \tag{4}$$

Here, $F_k^{(j)}(t)$ denotes the interaction force between the kth axle of the jth vehicle, which is at time t at the axle position $x_k^{(j)}(t) = vt - l_k^{(j)} - L_0$, with $l_k^{(j)}$ being the initial distance from the left support of the track at $x = -L_0$, as shown in Figs. 1 and 2. Consequently, the kth axle of the jth vehicle arrives at the track model at time instance $t_{Ak}^{(j)} = l_k^{(j)}/v$ and leaves the track at time $t_{Dk}^{(j)} = (l_k^{(j)} + 2L_0 + L_b)/v$. The Dirac delta function $\delta\left(x - x_k^{(j)}(t)\right)$ defines the position of $F_k^{(j)}(t)$ at $x_k^{(j)}(t)$, and the window function $\Pi(t, t_{Ak}^{(j)}, t_{Dk}^{(j)}) = H(t - t_{Ak}^{(j)}) - H(t - t_{Dk}^{(j)})$ controls the time range in which $F_k^{(j)}(t)$ crosses the track beam. The variable $n_a^{(j)}$ denotes the number of axle loads of the jth vehicle (note that for the considered conventional train $n_a^{(j)} = 4$ and $k = 1, 2, 3, 4$).

The boundary value problem is completed by the pinned boundary conditions of the track model,

$$\begin{aligned} w_r\left(x = -L_0, t\right) = 0, \quad w_r\left(x = L_b + L_0, t\right) = 0 \\ w_{r,xx}\left(x = -L_0, t\right) = 0, \quad w_{r,xx}\left(x = L_b + L_0, t\right) = 0. \end{aligned} \tag{5}$$

3.2 Bridge–soil subsystem

The half-space (soil) below the vertically excited rigid bridge foundations is represented in a simplified manner by spring–damper elements [11] located below the bridge bearings, as shown in Fig. 1. Assuming that the half-space is homogeneous, the spring stiffness k_b and the viscous damping parameter c_b of these elements can be estimated, for instance, based on the Wolf cone model [39],

$$k_b = \frac{\rho_s c_w^2 A_0}{z_0} \ , \quad c_b = \rho_s c_w A_0, \tag{6}$$

where

$$z_0 = \frac{\pi}{4} (1 - \nu) \left(\frac{c_w}{c_s}\right)^2 r_0. \tag{7}$$

ρ_s is the density of the soil, A_0 the contact area of the foundation, $r_0 = \sqrt{A_0/\pi}$ the equivalent radius of a circular plate with the same area as the foundation, and $c_s = \sqrt{G/\rho_s}$ the shear velocity with G denoting the shear modulus of the soil. Depending on *Poisson*'s ratio ν of the subsoil, the variable c_w is either equal to the compression wave velocity c_p or twice the shear wave velocity c_s of the homogeneous half-space,

$$c_w = \begin{cases} c_p = \sqrt{\frac{E_s}{\rho_s}} & \nu \leq 1/3 \\ 2c_s = 2\sqrt{\frac{G}{\rho_s}} & 1/3 < \nu \leq 1/2 \end{cases}, \tag{8}$$

with the constrained modulus E_s of soil, which is related to the shear modulus G by $E_s = 2G(1-\nu)/(1-2\nu)$. The dynamic stiffness decreases with increasing frequency, but since the stiffness coefficient k_b is a static quantity, for soils with a Poisson's ratio $\nu > 1/3$, additionally the lumped mass $\tilde{m}_g$ must be considered [39],

$$\tilde{m}_g = \frac{2.4}{\sqrt{\pi}} \left(\nu - \frac{1}{3}\right) \rho_s A_0^{(3/2)}. \tag{9}$$

The lumped mass m_b located at both bridge bearings represents thus the mass of the bridge foundations $\tilde{m}_1$, the mass of the soil above the foundations $\tilde{m}_2$, and the lumped soil mass $\tilde{m}_g$, i.e., $m_b = \tilde{m}_1 + \tilde{m}_2 + \tilde{m}_g$.

The vertical displacement $w_b(x, t)$ of the Euler–Bernoulli beam with constant mass per unit length ρA_b and constant flexural rigidity EI_b satisfies the following partial differential equation [9] in the range $0 \leq x \leq L_b$:

$$\rho A_b \ddot{w}_b(x, t) + EI_b w_{b,xxxx}(x, t) = q_b(x, t), \tag{10}$$

where

$$q_b(x, t) = k_f(x) \left(w_r(x, t) - w_b(x, t)\right) + c_f(x) \left(\dot{w}_r(x, t) - \dot{w}_b(x, t)\right) \tag{11}$$

is the force that is transferred to the bridge via the viscoelastic Winkler bedding, as shown in Fig. 2. The corresponding boundary conditions of the present beam problem are [20]

$$\begin{aligned} (x = 0): \quad & m_b \ddot{w}_b(0, t) + c_b \dot{w}_b(0, t) + k_b w_b(0, t) + EI_b w_{b,xxx}(0, t) = 0, \\ & w_{b,xx}(0, t) = 0, \\ (x = L_b): \quad & m_b \ddot{w}_b(L_b, t) + c_b \dot{w}_b(L_b, t) + k_b w_b(L_b, t) - EI_b w_{b,xxx}(L_b, t) = 0, \\ & w_{b,xx}(L_b, t) = 0. \end{aligned} \tag{12}$$

3.3 Train subsystem

The planar model of the jth vehicle of the considered conventional train is composed of seven rigid bodies with mass, i.e., the car body (subscript "p"), two bogies (subscript "s"), and four axles (subscript "a"), which are connected by spring–damper elements, as shown in Fig. 1. The model with a total of 10 DOFs has three rotational DOFs (rotation of the car body $\varphi_p^{(j)}$ and of the bogies $\varphi_{s1}^{(j)}$ and $\varphi_{s2}^{(j)}$) and seven translational DOFs (vertical axle displacements $u_{a1}^{(j)}, u_{a2}^{(j)}, u_{a3}^{(j)}, u_{a4}^{(j)}$; vertical displacement of the center of gravity of the car body

$u_{\mathrm{p}}^{(j)}$; vertical displacement of the center of gravity of the bogies $u_{\mathrm{s}1}^{(j)}$, $u_{\mathrm{s}2}^{(j)}$) [23,27], which are combined in the vector $\mathbf{u}_{\mathrm{c}}^{(j)}$,

$$\mathbf{u}_{\mathrm{c}}^{(j)} = \left[u_{\mathrm{p}}^{(j)}, \varphi_{\mathrm{p}}^{(j)}, u_{\mathrm{s}1}^{(j)}, \varphi_{\mathrm{s}1}^{(j)}, u_{\mathrm{s}2}^{(j)}, \varphi_{\mathrm{s}2}^{(j)}, u_{\mathrm{a}1}^{(j)}, u_{\mathrm{a}2}^{(j)}, u_{\mathrm{a}3}^{(j)}, u_{\mathrm{a}4}^{(j)} \right]^{\mathrm{T}}. \tag{13}$$

Neglecting the horizontal interaction between the N_{c} individual vehicles, the combined equations of motion of the complete train can be written as [31]

$$\mathbf{M}_{\mathrm{c}}\ddot{\mathbf{u}}_{\mathrm{c}} + \mathbf{C}_{\mathrm{c}}\dot{\mathbf{u}}_{\mathrm{c}} + \mathbf{K}_{\mathrm{c}}\mathbf{u}_{\mathrm{c}} = \mathbf{F}_{\mathrm{c}}, \tag{14}$$

with $\mathbf{M}_{\mathrm{c}}$, $\mathbf{C}_{\mathrm{c}}$, and $\mathbf{K}_{\mathrm{c}}$ being the mass, damping, and stiffness matrices of the train resulting from the individual system matrices of each vehicle,

$$\begin{aligned}
\mathbf{M}_{\mathrm{c}} &= \mathrm{diag}\left[\mathbf{M}_{\mathrm{c}}^{(1)}, \ldots, \mathbf{M}_{\mathrm{c}}^{(j)}, \ldots, \mathbf{M}_{\mathrm{c}}^{(N_{\mathrm{c}})} \right], \\
\mathbf{C}_{\mathrm{c}} &= \mathrm{diag}\left[\mathbf{C}_{\mathrm{c}}^{(1)}, \ldots, \mathbf{C}_{\mathrm{c}}^{(j)}, \ldots, \mathbf{C}_{\mathrm{c}}^{(N_{\mathrm{c}})} \right], \\
\mathbf{K}_{\mathrm{c}} &= \mathrm{diag}\left[\mathbf{K}_{\mathrm{c}}^{(1)}, \ldots, \mathbf{K}_{\mathrm{c}}^{(j)}, \ldots, \mathbf{K}_{\mathrm{c}}^{(N_{\mathrm{c}})} \right], \\
\mathbf{u}_{\mathrm{c}} &= \left[\mathbf{u}_{\mathrm{c}}^{(1)}, \ldots, \mathbf{u}_{\mathrm{c}}^{(j)}, \ldots, \mathbf{u}_{\mathrm{c}}^{(N_{\mathrm{c}})} \right]^{\mathrm{T}}.
\end{aligned} \tag{15}$$

The vehicle system matrices $\mathbf{M}_{\mathrm{c}}^{(j)}$, $\mathbf{C}_{\mathrm{c}}^{(j)}$, $\mathbf{K}_{\mathrm{c}}^{(j)}$ can be found in [20,31]. The force vector

$$\mathbf{F}_{\mathrm{c}} = \left[\mathbf{F}_{\mathrm{c}}^{(1)}, \mathbf{F}_{\mathrm{c}}^{(2)}, \ldots, \mathbf{F}_{\mathrm{c}}^{(N_{\mathrm{c}})} \right]^{\mathrm{T}} \tag{16}$$

is composed of the individual interaction force vectors (Fig. 1)

$$\mathbf{F}_{\mathrm{c}}^{(j)} = \left[0, 0, 0, 0, 0, 0, F_{\mathrm{as}}^{(j)} + F_{\mathrm{a}1}^{(j)}, F_{\mathrm{as}}^{(j)} + F_{\mathrm{a}2}^{(j)}, F_{\mathrm{as}}^{(j)} + F_{\mathrm{a}3}^{(j)}, F_{\mathrm{as}}^{(j)} + F_{\mathrm{a}4}^{(j)} \right]^{\mathrm{T}} \tag{17}$$

between the vehicle and the rail substructures at the position of each axle of the N_{c} vehicles. Each interaction force in turn consists of a dynamic component, $F_{\mathrm{a}k}^{(j)}$ ($k = 1, \ldots, 4$), and a static component $F_{\mathrm{as}}^{(j)}$,

$$F_{\mathrm{as}}^{(j)} = \frac{g}{4}\left(m_{\mathrm{p}}^{(j)} + 2m_{\mathrm{s}}^{(j)} + 4m_{\mathrm{a}}^{(j)} \right), \tag{18}$$

which is simply the gravity load of the vehicle distributed over the four axles, with g denoting the acceleration of gravity. In state space, the equations of motion of the train (Eq. 15) become [20]

$$\mathbf{A}_{\mathrm{c}}\dot{\mathbf{d}}_{\mathrm{c}} + \mathbf{B}_{\mathrm{c}}\mathbf{d}_{\mathrm{c}} = \mathbf{f}_{\mathrm{c}}, \tag{19}$$

with

$$\mathbf{A}_{\mathrm{c}} = \begin{bmatrix} \mathbf{C}_{\mathrm{c}} & \mathbf{M}_{\mathrm{c}} \\ \mathbf{M}_{\mathrm{c}} & \mathbf{0} \end{bmatrix}, \quad \mathbf{B}_{\mathrm{c}} = \begin{bmatrix} \mathbf{K}_{\mathrm{c}} & \mathbf{0} \\ \mathbf{0} & -\mathbf{M}_{\mathrm{c}} \end{bmatrix}, \quad \mathbf{f}_{\mathrm{c}} = \begin{bmatrix} \mathbf{F}_{\mathrm{c}} \\ \mathbf{0} \end{bmatrix}, \quad \mathbf{d}_{\mathrm{c}} = \begin{bmatrix} \mathbf{u}_{\mathrm{c}} \\ \dot{\mathbf{u}}_{\mathrm{c}} \end{bmatrix}. \tag{20}$$

4 Coupling of the bridge–soil and the track subsystems

The coupling of the bridge–soil subsystem with the track subsystem is achieved by CMS as proposed in [2]. The basis for the application of CMS is the modal expansion of the deformations of these substructures using the substructure eigenfunctions. The underlying modal properties of the non-classically damped subsystems are given in Appendix A (bridge–soil subsystem) and B (track subsystem).
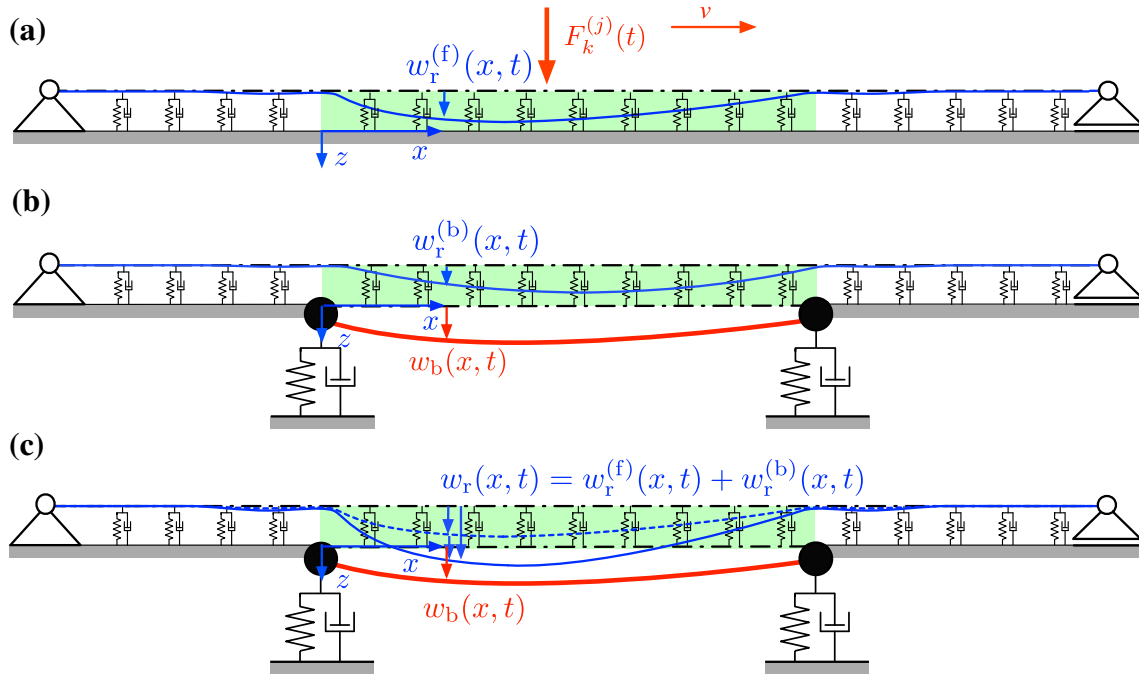
Fig. 3 a Track deflection $w_r^{(f)}(x, t)$ due to the interaction force $F_k^{(j)}(t)$. **b** Track deflection $w_r^{(b)}(x, t)$ resulting from the bridge displacement $w_b(x, t)$. **c** System with total deflection of the rail $w_r(x, t)$ and bridge displacement $w_b(x, t)$

4.1 Series expansion of the response variables

The response of the bridge–soil subsystem is approximated by the expansion of w_b into N_b complex modes of the corresponding stand-alone viscoelastically supported beam model,

$$w_b(x, t) \approx \sum_{m=1}^{N_b} y_b^{(m)}(t) \Phi_b^{(m)}(x) + \sum_{m=1}^{N_b} \bar{y}_b^{(m)}(t) \bar{\Phi}_b^{(m)}(x). \tag{21}$$

In Eq. (21), $\Phi_b^{(m)}(x)$ is the mth complex eigenfunction (see Eq. (54), Appendix A) and $y_b^{(m)}$ the mth modal coordinate of the stand-alone viscoelastically supported bridge beam, and $\bar{\Phi}_b^{(m)}(x)$ and $\bar{y}_b^{(m)}$ are the complex conjugate equivalents.

The applied CMS is based on a separation of the track displacement $w_r(x, t)$ into two parts [3],

$$w_r(x, t) = w_r^{(f)}(x, t) + w_r^{(b)}(x, t), \tag{22}$$

where $w_r^{(f)}(x, t)$ is the response of the track fixed at the interface with the bridge substructure due to the forcing function $f_r(x, t)$ and is thus governed by the equation of motion (Eq. (2)) without the quantities related to the bridge displacement w_b. Accordingly, $w_r^{(f)}(x, t)$ is approximated by the modal series

$$w_r^{(f)}(x, t) \approx \sum_{n=1}^{N_r} y_r^{(n)}(t) \Phi_r^{(n)}(x) + \sum_{n=1}^{N_r} \bar{y}_r^{(n)}(t) \bar{\Phi}_r^{(n)}(x) \tag{23}$$

using the first N_r complex eigenfunctions of the track substructure $\Phi_r^{(n)}(x), n = 1, \ldots, N_r$ (Eqs. (65) and (72), Appendix B). $y_r^{(n)}$ and $\bar{y}_r^{(n)}$ denote the nth modal coordinate of the track subsystem and its complex conjugate, respectively.

The second portion $w_r^{(b)}(x, t)$ denotes the track response induced by the displacement of the bedding at the interface to the bridge beam (i.e., the bridge displacement w_b) [3]. Figure 3 shows the idea of this separation graphically.

As discussed in [3], the response contribution $w_r^{(b)}$ is expressed by a series expansion based on the modal coordinates of the bridge $y_b^{(m)}(t)$ and $\bar{y}_b^{(m)}(t)$,

$$w_r^{(b)}(x,t) \approx \sum_{m=1}^{N_b} y_b^{(m)}(t) \Psi_r^{(m)}(x) + \sum_{m=1}^{N_b} \bar{y}_b^{(m)}(t) \bar{\Psi}_r^{(m)}(x), \tag{24}$$

with $\Psi_r^{(m)}(x)$ and $\bar{\Psi}_r^{(m)}(x)$ denoting the mth shape function of the track and its complex conjugate, respectively. An appropriate shape function can be derived from the mth eigenfunction $\Phi_b^{(m)}(x)$ of the bridge substructure by dropping f_r and the time-dependent terms in Eqs. (2) and (3) and inserting the mth modal contribution of $w_r^{(b)}$ and w_b, i.e., $w_r^{(b)(m)}(x,t) = \Psi_r^{(m)}(x)y_b^{(m)}(t)$ and $w_b^{(m)}(x,t) = \Phi_b^{(m)}(x)y_b^{(m)}(t)$. This yields the following quasi-static relationship between $\Psi_r^{(m)}(x)$ and $\Phi_b^{(m)}(x)$ in the form of an ordinary differential equation of the fourth order,

$$EI_r\Psi_{r,xxxx}^{(m)}(x) + k_f(x)\Psi_r^{(m)}(x) = k_f(x)\Phi_b^{(m)}(x)\Pi(x,0,L_b). \tag{25}$$

Equation (25) is solved numerically in combination with the boundary conditions of the track substructure (Eq. (5)). The corresponding complex conjugate $\bar{\Psi}_r^{(m)}$ is related to $\bar{\Phi}_b^{(m)}$ accordingly.

4.2 Component mode synthesis

In the initial step, the equations of motion of the bridge–soil and the track subsystems, as shown in Eq. (2) and Eq. (10), are rewritten as

$$\begin{bmatrix} \rho A_b & 0 \\ 0 & \rho A_r \end{bmatrix} \begin{bmatrix} \ddot{w}_b(x,t) \\ \ddot{w}_r(x,t) \end{bmatrix} + \begin{bmatrix} EI_b & 0 \\ 0 & EI_r \end{bmatrix} \begin{bmatrix} w_{b,xxxx}(x,t) \\ w_{r,xxxx}(x,t) \end{bmatrix}$$
$$= \begin{bmatrix} -k_f & k_f \\ k_f & -k_f \end{bmatrix} \begin{bmatrix} w_b(x,t) \\ w_r(x,t) \end{bmatrix} + \begin{bmatrix} -c_f & c_f \\ c_f & -c_f \end{bmatrix} \begin{bmatrix} \dot{w}_b(x,t) \\ \dot{w}_r(x,t) \end{bmatrix} + \begin{bmatrix} 0 \\ f_r \end{bmatrix}. \tag{26}$$

The series approximations of the response variables w_b, $w_r^{(b)}$, and $w_r^{(f)}$, shown in Eqs. (21), (23), and (24), are also written in a compact manner,

$$\begin{bmatrix} w_b(x,t) \\ w_r(x,t) \end{bmatrix} = \begin{bmatrix} w_b(x,t) \\ w_r^{(b)}(x,t) + w_r^{(f)}(x,t) \end{bmatrix} = \boldsymbol{\Lambda}\mathbf{h}_B, \tag{27}$$

with

$$\boldsymbol{\Lambda} = \begin{bmatrix} \boldsymbol{\Phi}_b(x)^T & \mathbf{0} \\ \boldsymbol{\Psi}_r(x)^T & \boldsymbol{\Phi}_r(x)^T \end{bmatrix}, \quad \mathbf{h}_B = \begin{bmatrix} \mathbf{y}_b(t) \\ \mathbf{y}_r(t) \end{bmatrix}. \tag{28}$$

The matrix $\boldsymbol{\Lambda}$ is composed of the vector $\boldsymbol{\Phi}_b(x)$ of the complex eigenfunctions of the bridge–soil subsystem, the vector $\boldsymbol{\Phi}_r(x)$ of the complex eigenfunctions of the track subsystem, and the vector $\boldsymbol{\Psi}_r(x)$ of the shape functions,

$$\boldsymbol{\Phi}_b = \left[\Phi_b^{(1)}, \Phi_b^{(2)}, \ldots, \Phi_b^{(N_b)}, \bar{\Phi}_b^{(1)}, \bar{\Phi}_b^{(2)}, \ldots, \bar{\Phi}_b^{(N_b)}\right]^T,$$
$$\boldsymbol{\Phi}_r = \left[\Phi_r^{(1)}, \Phi_r^{(2)}, \ldots, \Phi_r^{(N_r)}, \bar{\Phi}_r^{(1)}, \bar{\Phi}_r^{(2)}, \ldots, \bar{\Phi}_r^{(N_r)}\right]^T, \tag{29}$$
$$\boldsymbol{\Psi}_r = \left[\Psi_r^{(1)}, \Psi_r^{(2)}, \ldots, \Psi_r^{(N_b)}, \bar{\Psi}_r^{(1)}, \bar{\Psi}_r^{(2)}, \ldots, \bar{\Psi}_r^{(N_b)}\right]^T.$$

The vector $\mathbf{h}_B$ combines the two vectors $\mathbf{y}_b(t)$ and $\mathbf{y}_r(t)$ of the subsystem modal coordinates,

$$\mathbf{y}_b = \left[y_b^{(1)}, y_b^{(2)}, \ldots, y_b^{(N_b)}, \bar{y}_b^{(1)}, \bar{y}_b^{(2)}, \ldots, \bar{y}_b^{(N_b)}\right]^T,$$
$$\mathbf{y}_r = \left[y_r^{(1)}, y_r^{(2)}, \ldots, y_r^{(N_r)}, \bar{y}_r^{(1)}, \bar{y}_r^{(2)}, \ldots, \bar{y}_r^{(N_r)}\right]^T. \tag{30}$$

In the second step, in the combined equations of motion of the bridge–soil and the track subsystems (Eq. (26)) the response variables are substituted by the series approximation specified in Eq. (27). Subsequent

pre-multiplication by $\mathbf{\Lambda}^\mathrm{T}$, and integration over the track length $-L_0 \leq x \leq L_\mathrm{b} + L_0$ leads with the relation between the modal accelerations and velocities [20,28],

$$\begin{bmatrix} \ddot{\mathbf{y}}_\mathrm{b} \\ \ddot{\mathbf{y}}_\mathrm{r} \end{bmatrix} = \begin{bmatrix} \mathbf{S}_\mathrm{b}\dot{\mathbf{y}}_\mathrm{b} \\ \mathbf{S}_\mathrm{r}\dot{\mathbf{y}}_\mathrm{r} \end{bmatrix} \tag{31}$$

$$\mathbf{S}_\mathrm{b} = \mathrm{diag}\left[s_\mathrm{b}^{(1)}, s_\mathrm{b}^{(2)}, \dots, s_\mathrm{b}^{(N_\mathrm{b})}, \bar{s}_\mathrm{b}^{(1)}, \bar{s}_\mathrm{b}^{(2)}, \dots, \bar{s}_\mathrm{b}^{(N_\mathrm{b})}\right],$$

$$\mathbf{S}_\mathrm{r} = \mathrm{diag}\left[s_\mathrm{r}^{(1)}, s_\mathrm{r}^{(2)}, \dots, s_\mathrm{r}^{(N_\mathrm{r})}, \bar{s}_\mathrm{r}^{(1)}, \bar{s}_\mathrm{r}^{(2)}, \dots, \bar{s}_\mathrm{r}^{(N_\mathrm{r})}\right] \tag{32}$$

finally to the following coupled set of equations track–bridge–soil subsystem in terms of its modal coordinates,

$$\mathbf{A}_\mathrm{B}\dot{\mathbf{h}}_\mathrm{B} + \mathbf{B}_\mathrm{B}\mathbf{h}_\mathrm{B} = \mathbf{f}_\mathrm{B}. \tag{33}$$

The members of the diagonal matrices $\mathbf{S}_\mathrm{b}$ and $\mathbf{S}_\mathrm{r}$: $s_\mathrm{b}^{(m)}, \bar{s}_\mathrm{b}^{(m)}, m = 1, \dots, N_\mathrm{b}$; $s_\mathrm{r}^{(n)}, \bar{s}_\mathrm{r}^{(n)}, n = 1, \dots, N_\mathrm{r}$, are the complex natural frequencies of the bridge–soil and track substructures and their complex conjugate counterparts, respectively (see Appendices A and B). The system matrices $\mathbf{A}_\mathrm{B}$ and $\mathbf{B}_\mathrm{B}$,

$$\mathbf{A}_\mathrm{B} = \begin{bmatrix} \mathbf{A}_\mathrm{b} + \Delta\mathbf{M}_\mathrm{b}\mathbf{S}_\mathrm{b} + \Delta\mathbf{C}_\mathrm{b} & \mathbf{M}_\mathrm{br}\mathbf{S}_\mathrm{r} + \mathbf{C}_\mathrm{br} \\ \mathbf{M}_\mathrm{rb}\mathbf{S}_\mathrm{b} + \mathbf{C}_\mathrm{rb} & \mathbf{A}_\mathrm{r} \end{bmatrix},$$

$$\mathbf{B}_\mathrm{B} = \begin{bmatrix} \mathbf{B}_\mathrm{b} + \Delta\mathbf{K}_\mathrm{b} & \mathbf{0} \\ \mathbf{0} & \mathbf{B}_\mathrm{r} \end{bmatrix}, \tag{34}$$

are composed of several sub-matrices, which are explained in the following. The two diagonal sub-matrices $\mathbf{A}_\mathrm{b}$ and $\mathbf{B}_\mathrm{b}$ contain the coefficients for the orthogonality conditions of the eigenfunctions of the bridge–soil subsystem $a_\mathrm{b}^{(m)}, \bar{a}_\mathrm{b}^{(m)}, b_\mathrm{b}^{(m)}, \bar{b}_\mathrm{b}^{(m)}, m = 1, \dots, N_\mathrm{b}$,

$$\mathbf{A}_\mathrm{b} = \mathrm{diag}\left[a_\mathrm{b}^{(1)}, a_\mathrm{b}^{(2)}, \dots, a_\mathrm{b}^{(N_\mathrm{b})}, \bar{a}_\mathrm{b}^{(1)}, \bar{a}_\mathrm{b}^{(2)}, \dots, \bar{a}_\mathrm{b}^{(N_\mathrm{b})}\right],$$

$$\mathbf{B}_\mathrm{b} = \mathrm{diag}\left[b_\mathrm{b}^{(1)}, b_\mathrm{b}^{(2)}, \dots, b_\mathrm{b}^{(N_\mathrm{b})}, \bar{b}_\mathrm{b}^{(1)}, \bar{b}_\mathrm{b}^{(2)}, \dots, \bar{b}_\mathrm{b}^{(N_\mathrm{b})}\right], \tag{35}$$

described in detail in Appendix A. The corresponding matrices for the stand-alone track subsystem, $\mathbf{A}_\mathrm{r}$ and $\mathbf{B}_\mathrm{r}$, read as

$$\mathbf{A}_\mathrm{r} = \mathrm{diag}\left[a_\mathrm{r}^{(1)}, a_\mathrm{r}^{(2)}, \dots, a_\mathrm{r}^{(N_\mathrm{r})}, \bar{a}_\mathrm{r}^{(1)}, \bar{a}_\mathrm{r}^{(2)}, \dots, \bar{a}_\mathrm{r}^{(N_\mathrm{r})}\right],$$

$$\mathbf{B}_\mathrm{r} = \mathrm{diag}\left[b_\mathrm{r}^{(1)}, b_\mathrm{r}^{(2)}, \dots, b_\mathrm{r}^{(N_\mathrm{r})}, \bar{b}_\mathrm{r}^{(1)}, \bar{b}_\mathrm{r}^{(2)}, \dots, \bar{b}_\mathrm{r}^{(N_\mathrm{r})}\right]. \tag{36}$$

Details on the coefficients $a_\mathrm{r}^{(n)}, \bar{a}_\mathrm{r}^{(n)}, b_\mathrm{r}^{(n)}, \bar{b}_\mathrm{r}^{(n)}, n = 1, \dots, N_\mathrm{r}$, in these matrices are found in Appendix B. The sub-matrices $\Delta\mathbf{M}_\mathrm{b}, \Delta\mathbf{C}_\mathrm{b}$, and $\Delta\mathbf{K}_\mathrm{b}$ read as

$$\Delta\mathbf{M}_\mathrm{b} = \rho A_\mathrm{r} \int_{-L_0}^{L_b+L_0} \mathbf{\Psi}_\mathrm{r}\mathbf{\Psi}_\mathrm{r}^\mathrm{T}\mathrm{d}x,$$

$$\Delta\mathbf{C}_\mathrm{b} = -c_\mathrm{fb}\left(\int_0^{L_\mathrm{b}} \mathbf{\Phi}_\mathrm{b}\mathbf{\Psi}_\mathrm{r}^\mathrm{T}\mathrm{d}x + \left(\int_0^{L_\mathrm{b}} \mathbf{\Phi}_\mathrm{b}\mathbf{\Psi}_\mathrm{r}^\mathrm{T}\mathrm{d}x\right)^\mathrm{T}\right.$$

$$\left. - \int_0^{L_\mathrm{b}} \mathbf{\Phi}_\mathrm{b}\mathbf{\Phi}_\mathrm{b}^\mathrm{T}\mathrm{d}x \right) + \int_{-L_0}^{L_b+L_0} c_\mathrm{f}\mathbf{\Psi}_\mathrm{r}\mathbf{\Psi}_\mathrm{r}^\mathrm{T}\mathrm{d}x,$$

$$\Delta\mathbf{K}_\mathrm{b} = -k_\mathrm{fb}\left(\int_0^{L_\mathrm{b}} \mathbf{\Phi}_\mathrm{b}\mathbf{\Psi}_\mathrm{r}^\mathrm{T}\mathrm{d}x + \left(\int_0^{L_\mathrm{b}} \mathbf{\Phi}_\mathrm{b}\mathbf{\Psi}_\mathrm{r}^\mathrm{T}\mathrm{d}x\right)^\mathrm{T}\right.$$

$$\left. - \int_0^{L_\mathrm{b}} \mathbf{\Phi}_\mathrm{b}\mathbf{\Phi}_\mathrm{b}^\mathrm{T}\mathrm{d}x \right) + \int_{-L_0}^{L_b+L_0} k_\mathrm{f}\mathbf{\Psi}_\mathrm{r}\mathbf{\Psi}_\mathrm{r}^\mathrm{T}\mathrm{d}x$$

$$+ EI_\mathrm{r} \int_{-L_0}^{L_b+L_0} \mathbf{\Psi}_\mathrm{r}\mathbf{\Psi}_{\mathrm{r},xxxx}^\mathrm{T}\mathrm{d}x, \tag{37}$$

and the sub-matrices

$$
\mathbf{M}_{br} = \mathbf{M}_{rb}^{T} = \rho A_r \int_{-L_0}^{L_b+L_0} \boldsymbol{\Psi}_r \boldsymbol{\Phi}_r^{T} dx,
$$
$$
\mathbf{C}_{br} = \mathbf{C}_{rb}^{T} = \int_{-L_0}^{L_b+L_0} c_f \boldsymbol{\Psi}_r \boldsymbol{\Phi}_r^{T} dx - c_{fb} \int_{0}^{L_b} \boldsymbol{\Phi}_b \boldsymbol{\Phi}_r^{T} dx
\tag{38}
$$

result from coupling of the bridge–soil and the track subsystems.

The force vector $\mathbf{f}_B$ in Eq. (33),

$$
\mathbf{f}_B = \begin{bmatrix} \mathbf{f}_b \\ \mathbf{f}_r \end{bmatrix},
\tag{39}
$$

captures the effect of the vehicle interaction forces $F_k^{(j)}, j = 1, \ldots, N_c, k = 1, \ldots, 4$ (for the considered four axle vehicles), separately for the bridge–soil subsystem by the vector $\mathbf{f}_b$ and for the track subsystem by the vector $\mathbf{f}_r$. The vector $\mathbf{f}_b$ reads as

$$
\mathbf{f}_b = \sum_{j=1}^{N_c} \boldsymbol{\Psi}_r^{(j)} \boldsymbol{\Pi}^{(j)} \mathbf{F}^{(j)}, \quad \mathbf{F}^{(j)} = \left[F_1^{(j)}, F_2^{(j)}, F_3^{(j)}, F_4^{(j)} \right]^{T},
\tag{40}
$$

where

$$
\boldsymbol{\Pi}^{(j)} = \text{diag} \left[\Pi(t, t_{A1}^{(j)}, t_{D1}^{(j)}), \Pi(t, t_{A2}^{(j)}, t_{D2}^{(j)}), \Pi\left(t, t_{A3}^{(j)}, t_{D3}^{(j)}\right), \Pi\left(t, t_{A4}^{(j)}, t_{D4}^{(j)}\right) \right]
\tag{41}
$$

and

$$
\boldsymbol{\Psi}_r^{(j)} = \left[\boldsymbol{\Psi}_r\left(x_1^{(j)}\right), \boldsymbol{\Psi}_r\left(x_2^{(j)}\right), \boldsymbol{\Psi}_r\left(x_3^{(j)}\right), \boldsymbol{\Psi}_r\left(x_4^{(j)}\right) \right],
\tag{42}
$$

with $x_i^{(j)}$ ($i = 1, \ldots, 4$) corresponding to the axle position of each of the four axles of the jth vehicle. The vector $\mathbf{f}_r$ is computed according to

$$
\mathbf{f}_r = \sum_{j=1}^{N_c} \boldsymbol{\Phi}_r^{(j)} \boldsymbol{\Pi}^{(j)} \mathbf{F}^{(j)},
\tag{43}
$$

where

$$
\boldsymbol{\Phi}_r^{(j)} = \left[\boldsymbol{\Phi}_r\left(x_1^{(j)}\right), \boldsymbol{\Phi}_r\left(x_2^{(j)}\right), \boldsymbol{\Phi}_r\left(x_3^{(j)}\right), \boldsymbol{\Phi}_r\left(x_4^{(j)}\right) \right].
\tag{44}
$$

In case of a single load model, where interaction forces in $\mathbf{F}^{(j)}$ are assumed to be constant and of known value (i.e., the static axle loads of the train), Eq. (33) can be solved numerically by applying the fourth-order Runge–Kutta method [6].

5 Coupling of the track–bridge–soil and the train subsystems

First, the equations of motion of the track–bridge–soil subsystem, as shown in Eq. (33), and the train subsystem, as shown in Eq. (19), are written in a compact manner,

$$
\mathbf{A}^* \dot{\mathbf{x}}^*(t) + \mathbf{B}^* \mathbf{x}^*(t) = \mathbf{f}^*(t),
\tag{45}
$$

where

$$
\mathbf{A}^* = \text{diag}\left[\mathbf{A}_B, \mathbf{A}_c\right], \quad \mathbf{B}^* = \text{diag}\left[\mathbf{B}_B, \mathbf{B}_c\right], \quad \mathbf{x}^*(t) = \begin{bmatrix} \mathbf{h}_B \\ \mathbf{d}_c \end{bmatrix}, \quad \mathbf{f}^*(t) = \begin{bmatrix} \mathbf{f}_B \\ \mathbf{f}_c \end{bmatrix}.
\tag{46}
$$

In Eq. (45), the DOFs at the interface of the two subsystems are still decoupled. The coupling of the axle and the rail displacements is achieved by the so-called *corresponding assumption* [45].

According to this assumption, the displacement of each axle of the train corresponds to the underlying rail displacement including track irregularity, as shown in Figs. 1 and 4. The wheels are thus assumed to be in rigid contact with the rails, and lift-off is not possible. Approximating the displacement of the track beam w_r by a modal series with N_r modes (Eq. (24)), the corresponding assumption yields the vertical displacement of the kth axle ($k = 1, \ldots, 4$)) of the jth vehicle at the position $x_k^{(j)}(t)$ as follows:

$$u_{ak}^{(j)}\left(x_k^{(j)}\right) = w_r\left(x_k^{(j)}, t\right) + I_{irr}\left(x_k^{(j)}\right)$$

$$\approx \sum_{n=1}^{N_r} \Phi_r^{(n)}\left(x_k^{(j)}\right) y_r^{(n)}(t) + \sum_{n=1}^{N_r} \bar{\Phi}_r^{(n)}\left(x_k^{(j)}\right) \bar{y}_r^{(n)}(t)$$

$$+ \sum_{m=1}^{N_b} \Psi_r^{(m)}\left(x_k^{(j)}\right) y_b^{(m)}(t) + \sum_{m=1}^{N_b} \bar{\Psi}_r^{(m)}\left(x_k^{(j)}\right) \bar{y}_b^{(m)}(t) + I_{irr}\left(x_k^{(j)}\right). \quad (47)$$

The variable I_{irr} denotes a random irregularity profile function, which is applied to the track surface, to consider track irregularities, as shown in Fig. 4. The generation of the random irregularity functions is based on power spectral density functions, as described in detail in [8]. The corresponding expressions for the axle velocity and axle acceleration, as shown in Eqs. (76) and (77), are specified in Appendix C. These relations leave the DOFs of the axles and the modal coordinates of the track coupled.

According to the corresponding assumption, the interaction forces between the track beam and the vehicle are equal. Thus, for example, the axle force $F_{ak}^{(j)}(t)$ corresponds to the interaction force $F_k^{(j)}(t)$ on the track (Fig. 1).

The compatibility conditions Eqs. (47), (76), and (77) allow the application of a DST by condensation of the DOFs involved in these relations into the modal coordinates of the track beam substructure. This condensation reads as

$$\mathbf{x}^*(t) = \mathbf{\Gamma}_1(t)\mathbf{x}(t) + \mathbf{\Gamma}_2(t)\dot{\mathbf{x}}(t) + \mathbf{\Upsilon}(t), \quad \mathbf{x}(t) = \left[\mathbf{h}_b, \tilde{\mathbf{d}}_c\right]^{\mathrm{T}},$$

$$\dot{\mathbf{x}}^*(t) = \dot{\mathbf{\Gamma}}_1(t)\mathbf{x}(t) + \mathbf{\Gamma}_1(t)\dot{\mathbf{x}}(t) + \dot{\mathbf{\Gamma}}_2(t)\dot{\mathbf{x}}(t) + \mathbf{\Gamma}_2(t)\ddot{\mathbf{x}}(t) + \dot{\mathbf{\Upsilon}}(t), \quad (48)$$

with $\mathbf{\Gamma}_1(t)$ and $\mathbf{\Gamma}_2(t)$ serving as time-dependent transformation matrices and $\mathbf{\Upsilon}(t)$ including the irregularities of the track evaluated at the positions of the vehicle axis. These quantities are specified in Appendix C, Eqs. (78) and (79). The vector $\tilde{\mathbf{d}}_c$ is the vector $\mathbf{d}_c$ (see Eq. (20)) without the DOFs of the train axles. The transformation according to Eq. (48) imposes the corresponding assumption into the two subsystems, which are thus consolidated.

Next, Eq. (48) is inserted into Eq. (45) and pre-multiplied by $\mathbf{\Gamma}_1^{\mathrm{T}}(t)$, which leads to the combined equations of motion of the interacting track–bridge–soil–train system,

$$\mathbf{A}(t)\dot{\mathbf{x}}(t) + \mathbf{B}(t)\mathbf{x}(t) = \mathbf{f}(t), \quad (49)$$

where

$$\mathbf{A}(t) = \mathbf{\Gamma}_1^{\mathrm{T}}(t)\left(\mathbf{A}^*\mathbf{\Gamma}_1(t) + \mathbf{A}^*\dot{\mathbf{\Gamma}}_2(t) + \mathbf{A}^*\mathbf{\Gamma}_2(t)\mathbf{S} + \mathbf{B}^*\mathbf{\Gamma}_2(t)\right),$$

$$\mathbf{B}(t) = \mathbf{\Gamma}_1^{\mathrm{T}}(t)\left(\mathbf{A}^*\dot{\mathbf{\Gamma}}_1(t) + \mathbf{B}^*\mathbf{\Gamma}_1(t)\right), \quad (50)$$

$$\mathbf{f}(t) = \mathbf{\Gamma}_1^{\mathrm{T}}(t)\left(\mathbf{f}^*(t) - \mathbf{A}^*\dot{\mathbf{\Upsilon}}(t) - \mathbf{B}^*\mathbf{\Upsilon}(t)\right).$$

In the matrix $\mathbf{S}$,

$$\mathbf{S} = \mathrm{diag}\left[\mathbf{S}_b, \mathbf{S}_r, \mathbf{I}_{N_c}\frac{\mathrm{d}}{\mathrm{d}t}\right]. \quad (51)$$
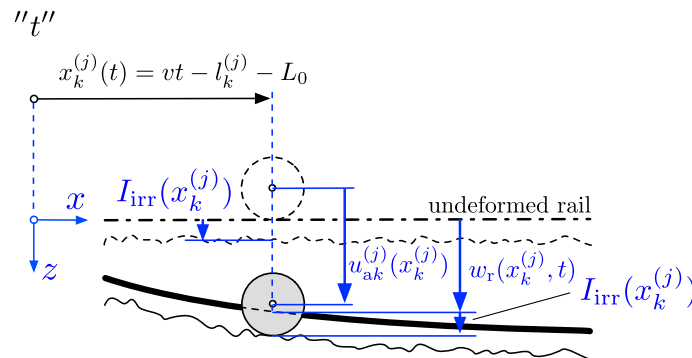
Fig. 4 Corresponding assumption coupling axle and rail displacements (modified from [20])

track: modal parameters
$s_r^{(n)}$, $\bar{s}_r^{(n)}$ (Eq. (67))
$\Phi_r^{(n)}$, $\bar{\Phi}_r^{(n)}$ (Eq. (65))

bridge: modal parameters
$s_b^{(m)}$, $\bar{s}_b^{(m)}$ (Eq. (55))
$\Phi_b^{(m)}$, $\bar{\Phi}_b^{(m)}$ (Eq. (54))

shapefunctions
$\Psi_r^{(m)}$, $\bar{\Psi}_r^{(m)}$, Eq. (25)

time-independent matrices
$\mathbf{A}_B$, $\mathbf{B}_B$, Eq. (34)

time-step t_i:
- time-dependent matrices
$\mathbf{A}(t_i)$, $\mathbf{B}(t_i)$, Eq. (50)
- Solution of Eq. (49) for $\mathbf{x}(t_i)$
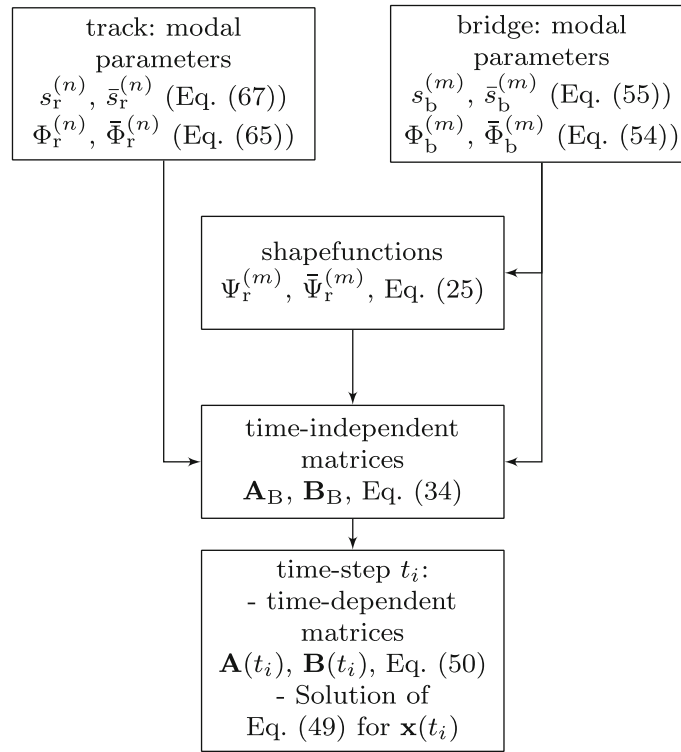
Fig. 5 Steps of the model implementation

Table 1 Properties of the soil/foundation and resulting parameters at the bridge boundaries

Properties soil/foundation			Parameters bridge-boundaries		
Variable	Value	Unit	Variable	Value	Unit
E_s	$2 \cdot 10^8$	N/m^2	k_b	$1.276 \cdot 10^9$	N/m
ν	0.3	–	c_b	$3.229 \cdot 10^7$	kg/s
ρ_s	2263	kg/m^3	m_b	$3 \cdot 10^5$	kg
A_0	48	m^2			
$\tilde{m}_1 + \tilde{m}_2$	$3 \cdot 10^5$	kg			

$\mathbf{I}_{N_c}$ denotes the identity matrix of order of the length of $\tilde{\mathbf{d}}_c$. Note that only the static axle loads (Eqs. (16) and (17)) remain in the force vector $\mathbf{f}(t)$, and the dynamic interaction forces $F_{ak}^{(j)}(t)$ and $F_k^{(j)}(t)$ cancel each other out when $\mathbf{f}^*(t)$ is pre-multiplied by $\Gamma_1^T(t)$. The coupled set of equations of motion (Eq. (49)) with time-dependent system matrices is solved by applying the Runge–Kutta method [6]. The steps involved with the solution procedure of the proposed model are summarized in Fig. 5.

6 Application

6.1 Validation

To validate the proposed semi-analytical modeling approach implemented in MATLAB [25], the results of an application example are compared with those of an FE model created in the software suite Abaqus [1]. To this end, a single-span bridge of length $L_b = 21$ m, flexural rigidity $EI_b = 2.6 \cdot 10^{10}$ Nm^2, and mass per unit length $\rho A_b = 7083$ kg/m, resting on a moderately stiffness soil with parameters given in Table 1 is considered.

From the soil parameters, by applying Eq. (6) the stiffness and damping coefficients of the spring and damper below the bridge ends are obtained as $k_b = 1.276 \cdot 10^9$ N/m^2 and $c_b = 3.229 \cdot 10^7$ Ns/m^2. Since the transient dynamical analysis in Abaqus does not use modal superposition, in the FE model modal damping
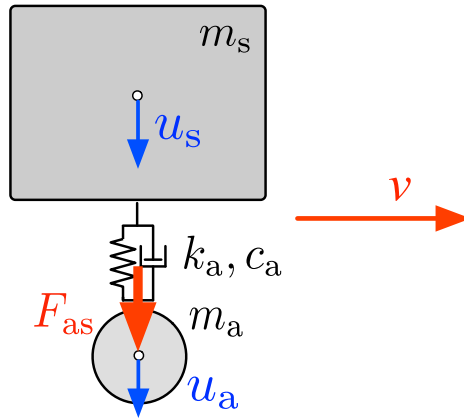
Fig. 6 Two-degree-of-freedom MSD system

Table 2 Parameters of two-degree-of-freedom ICE 3 train model [26]

Component	Variable	Value	Unit
1/4 car body mass + 1/2 bogie mass	m_s	15125	kg
Axle mass	m_a	1800	kg
Suspension stiffness	k_a	$1.764 \cdot 10^6$	N/m
Suspension damping	c_a	$4.800 \cdot 10^4$	Ns/m

cannot be implemented. Therefore, to ensure comparability of the results, structural damping is not considered in this example. The parameters of the track subsystem are as follows [3,7]: flexural rigidity $EI_r = 8.6 \cdot 10^6$ Nm^2, mass per unit length $\rho A_r = 103$ kg/m, bedding stiffness coefficient $k_f = 1.316 \cdot 10^8$ N/m^2, and bedding damping coefficient $c_f = 6.42 \cdot 10^4$ Ns/m^2. The length of the track before and after the bridge is chosen as $L_0 = 30$ m, which is much larger than the minimum value according to Eq. (1) (3.21 m). To capture track irregularities, the random irregularity profile $I_{irr}(x)$ shown in Fig. 7 is assigned to the rail. This irregularity profile was created by a stochastic superposition of J harmonic functions as described in [8] with the following input parameters: number of harmonic functions $J = 1000$, characteristic frequencies $\Omega_c = 0.8246$ rad/m, $\Omega_r = 0.0206$ rad/m, $\Omega_s = 0.4380$ rad/m, half distance between rails $l = 0.72$ m, factor for moderate rail quality $A = 1.0891 \cdot 10^{-6}$, spatial frequency range $[\pi/50, \pi]$ rad/m. For details on this procedure and the meaning of the input parameters, it is referred to [8].

In this validation example, the bridge–track system is crossed by the simple MSD system shown in Fig. 6 at constant speed $v = 80$ m/s. That is, instead of a full vehicle with four axles, this MSD system with parameters specified in Table 2 represents a single axle, half a bogie, and a quarter of a car body of a standard ICE 3 train [26]. The corresponding system matrices $\mathbf{A}_c$, $\mathbf{B}_c$, force vector $\mathbf{f}_c$, and vector of degrees of freedom $\mathbf{u}_c$ of Eq. (20) read as

$$\mathbf{A}_c = \begin{bmatrix} c_a & -c_a & m_s & 0 \\ -c_a & c_a & 0 & m_a \\ m_s & 0 & 0 & 0 \\ 0 & m_a & 0 & 0 \end{bmatrix},$$

$$\mathbf{B}_c = \begin{bmatrix} k_a & -k_a & 0 & 0 \\ -k_a & k_a & 0 & 0 \\ 0 & 0 & m_s & 0 \\ 0 & 0 & 0 & m_a \end{bmatrix}, \tag{52}$$

$$\mathbf{f}_c = \begin{bmatrix} 0 \\ F_{as} \\ 0 \\ 0 \end{bmatrix}, \quad \mathbf{u}_c = \begin{bmatrix} u_s \\ u_a \\ \dot{u}_s \\ \dot{u}_a \end{bmatrix}, \tag{53}$$

with F_{as} denoting the static axle load.

Table 3 First six natural complex frequencies of the considered bridge subsystem, the corresponding natural frequencies, and equivalent damping ratios. Natural frequencies of the simply supported bridge subsystem (last column)

Mode m	Complex nat. frequ. $s_b^{(m)}$ (rad/s)	Nat. frequency $f_b^{(m)}$ (Hz)	Damping ratio $\zeta_b^{(m)}$ (%)	Nat. frequency (ss) $f_b^{(m)}$ (Hz)
1	$-1.35 + 42.10i$	6.70	3.21	6.82
2	$-49.90 + 38.43i$	6.12	79.22	27.29
3	$-50.07 + 41.31i$	6.58	77.14	61.39
4	$-2.23 + 174.79i$	27.81	1.28	109.11
5	$-1.10 + 389.91i$	62.06	0.28	170.42
6	$-0.64 + 690.21i$	109.85	0.09	245.29
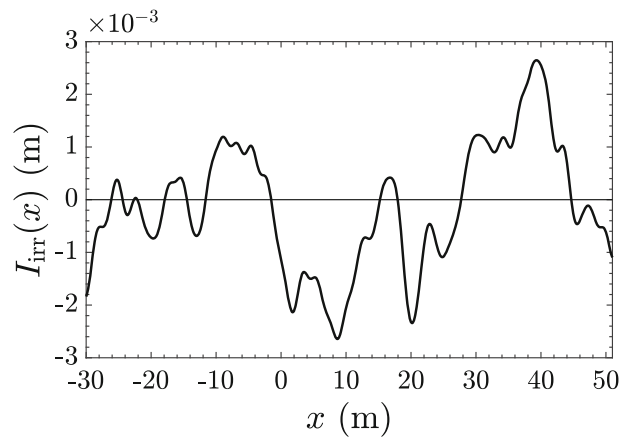
Fig. 7 Used irregularity profile

When computing the dynamic response using the proposed semi-analytical approach, $N_b = 8$ modes of the stand-alone bridge substructure are taken into account. In Table 3, the first six complex natural frequencies of these modes and the corresponding natural frequencies ($f_b^{(m)} = \Im\mathfrak{m}(s_b^{(m)})/2\pi = \Omega_b^{(m)}/2\pi$) and equivalent modal damping ratios due to the dashpot dampers at the beam ends are listed. As can be seen, the second and third modes are heavily damped with an equivalent damping ratio of close to 80%. In the last column of Table 3 also, the first six natural frequencies of the corresponding simply supported bridge (i.e., the subsoil is assumed to be rigid) are listed, showing that the two highly damped modes of the viscoelastically supported structure do not appear but instead the second natural frequency of the simply supported beam is almost identical with the fourth of the viscoelastically supported one.

With high values of the bedding coefficient k_f, the deflection and acceleration of the rail become very isolated around a single load leading to a high number of modes required to accurately describe the deformed shape if modal superposition is applied. This fact, albeit mentioned in the literature (e.g., [14]), is oftentimes overlooked when modal superposition is used in railway bridge dynamics and was not discussed in [3]. However, in the presence of track irregularities the modal series of the track substructure must be approximated by a significantly large number of these modes to correctly predict the bridge response. In the present validation example, up to $N_r = 200$ modes of the track subsystem are considered in the response analysis.

In the Abaqus FE model used for validation, the bridge and the track subsystems are discretized by Euler–Bernoulli beam elements of type B23 with an element size of 0.06125 m. To match the rail irregularity profile (Fig. 7) of the semi-analytical model, the element nodes of the rail beam are simply offset from the axis of the perfectly straight and smooth track by the amount of the irregularity at the corresponding position x. The viscoelastic bedding of the track is represented by a series of discrete spring and dashpot elements also spaced 0.06125 m apart. The MSD system is modeled as two rigid body lumped masses connected by discrete spring and dashpot elements. Since only the vertical motion of the two lumped masses is considered, the rotational DOFs of the lumped masses are constrained to be zero. The DOF in the horizontal direction is pre-defined by the speed $v = 80$ m/s and the initial position at the left support of the rail beam. The vertical DOF of the upper lumped mass is unconstrained, and the contact between axle mass and rail beam is achieved by a so-called *slide line*, which models the rigid connection according to the corresponding assumption.
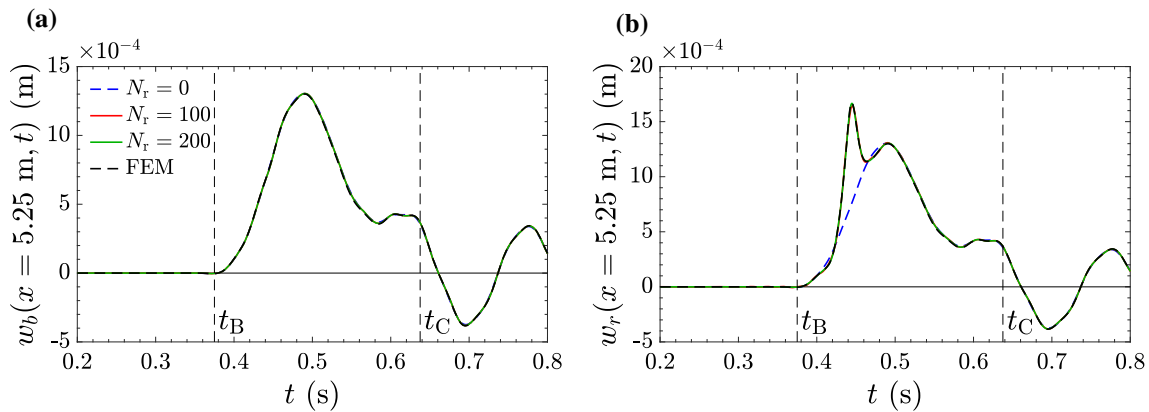
Fig. 8 **a** Bridge deflection, and **b** rail deflection at the position $x = 1/4L_b$

Figure 8a shows the vertical displacement of the bridge at the position $x = 1/4L_b$ and Fig. 8b the deflection of the rail at the same location in the time range from 0.2 to 0.8 s. Within this time frame, the MSD system enters the bridge at time $t_B = 0.375$ s and leaves it at time $t_C = 0.6375$ s. The black dashed line is the result of the analysis on the FE model, and the other lines show the response of the proposed model considering different numbers of modes N_r in approximating the dynamic response portion $w_r^{(f)}$ of the track subsystem according to Eq. (23). From Fig. 8a, it can be seen that the FE reference solution for the bridge displacement w_b and the solution of the proposed model are practically identical regardless of the number of rail modes N_r considered. Since even for $N_r = 0$ this response quantity is predicted very well (i.e., $w_r^{(f)} = 0$), the dynamic track response $w_r^{(f)}$ does not affect the vertical displacement of the bridge w_b. In contrast, for the prediction of the total track deflection w_r, $N_r = 100$ modes of the track substructure must be included in the approximation of $w_r^{(f)}$, so that the time history of the FE reference solution and that of the proposed model coincide, as shown in Fig. 8b.

Since in most cases the acceleration of the bridge deck is decisive for the assessment of the probability of failure of railway bridges under high-speed trains [22], the calculation of the bridge acceleration is of particular importance. Therefore, Fig. 9a shows this response quantity of the bridge and in Fig. 9b of the track at the same position in the same time frame. It can be seen that for the "exact" prediction of the bridge acceleration $N_r = 100$ modes of the tack subsystem are necessary. If the portion $w_r^{(f)}$ is neglected (i.e., $N_r = 0$), the maximum bridge acceleration of 1.33 m/s² is underestimated by about 15 %. In contrast, the adequate prediction of the track acceleration already requires $N_r = 200$ modes, since the acceleration at the point where the MSD system is currently located is almost singular. However, it should be noted that in general the track acceleration is of minor importance and is therefore not calculated. An underestimation of the bridge acceleration of a few percent is generally also not a problem. From this discussion, a major advantage of the proposed calculation methodology already becomes obvious, namely that the number of modes (and thus the number of degrees of freedom) of the two subsystems included in the calculation can be chosen differently and adapted to the problem.

From this first comparative study, it can be concluded that the proposed method can accurately and efficiently calculate the response of this model.

6.2 Example problem

To further investigate the capabilities of the proposed model, several comparative studies are performed. The bridge considered is the same as in the validation example; however, now a constant modal damping ratio of $\tilde{\zeta}_b^{(m)} = 0.5$ % ($m = 1, \ldots N_b$) is added to each mode of the bridge to account for structural damping. The structure is subjected to an ICE3 train composed of $N_c = 8$ vehicles, each modeled as a 10-DOF MSD system as depicted in Fig. 1. Each of the vehicles is considered identical, with parameters listed in Table 4 and variables referring to Fig. 1. A full list of all parameters of this train type can be found in [26], and for the system matrices $\mathbf{M}_c$, $\mathbf{C}_c$, $\mathbf{K}_c$ of the planar MSD system, it is referred to [20]. In the initial studies, a perfectly straight and smooth track is assumed (i.e., no track irregularities are taken into account).
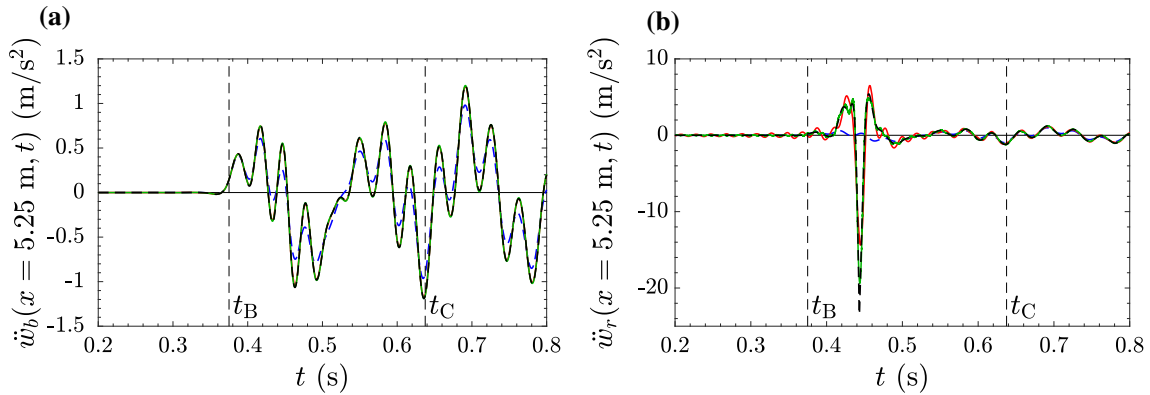
(a)

(b)

Fig. 9 a Bridge acceleration, and **b** rail acceleration at the position $x = 1/4 L_b$

Table 4 Parameters of the 10-DOF MSD vehicle model [26]

Parameter	Variables	Value	Unit
Mass	m_p, m_s, m_a	53500, 3500, 1800	kg
Mass moment of inertia	I_p, I_s	1690, 4.569	10^3kgm^2
Dimension	h_s, h_a	17.375, 2.5	m
Suspension stiffness	k_s, k_a	820, 17460	kN/m
Suspension damping	c_s, c_a	90, 48	kNs/m

As before, the beam response w_b is approximated by $N_b = 8$ series terms and thus also the contribution $w_r^{(b)}$ of the track deflection. In two different approaches, once in the series representation of the dynamic track deformation $w_r^{(f)}$ according to Eq. (23) $N_r = 100$ modes are considered, and the second time this response contribution is neglected, $w_r^{(f)} = 0$, i.e., $N_r = 0$. In a sequence of computations, the speed of the train is incrementally increased in the range 10 m/s $\leq v \leq$ 90 m/s, and the maximum bridge deflection and the maximum bridge acceleration are recorded and plotted against the speed. The resulting representation of the peak response as a function of v, referred to as response spectra, is shown in Fig. 10. Here, the results on the left, as shown in Fig. 10a, depict the maximum absolute beam deflection $\max|w_{b,rel}| = \max|(w_b(x, t) - (w_b(0, t) + x(w_b(L_b, t) - w_b(0, t))/L_b))|$, which corresponds to the vertical displacement without the rigid body displacement due to the support displacements. The right subfigure, as shown in Fig. 10b, contains the maximum absolute acceleration response of the bridge.

As can be observed, these response spectra exhibit local peaks related to resonance effects resulting from the regular axle spacing of the moving MSD system. These peaks are found close to the so-called resonance speeds, defined as $v_j^{(m)} = f_b^{(m)} d/j$ (j=1,2,3,...), which are directly related to the mth natural frequency of the bridge and the characteristic length of the train d [41]. The characteristic length indicates the distance at which the moving load pattern of the train repeats and corresponds to the vehicle length $d = 24.775$ m of the considered train. While this definition is exact in the case of a single load model (i.e., the train is represented only by its static axle loads) in combination with a bridge beam model without track, the observed peak values are slightly shifted as a result of the MSD train model due to the additional effects of train mass, damping, and stiffness. In Fig. 10b, some significant resonance speeds are specified, all associated with the first and fourth bridge modes, keeping in mind that for the viscoelastically supported bridge, the second and third modes (Table 3) do not induce resonance effects due to the strongly damped nature of these modes. The most important finding of this study is that the deflection of the bridge is virtually unaffected by setting $w_r^{(f)} = 0$, while the bridge acceleration is slightly overestimated only in the speed range between 65 and 76 m/s.

To illustrate the influence of soil properties on the bridge response, in Fig. 11 the outcomes of the viscoelastically supported structure (referred to as "flexibly supported") are compared with results of the corresponding simply supported bridge, i.e., the subsoil is assumed to be rigid (referred to as "rigidly supported"), both based on $N_r = 100$ modes for $w_r^{(f)}$. It can be clearly seen that, in wide speed ranges, both the deflection and acceleration are much larger for the rigidly supported bridge than for the bridge on a medium-stiff subsoil. This difference is particularly significant at resonance, and, for instance, at the maximum acceleration near
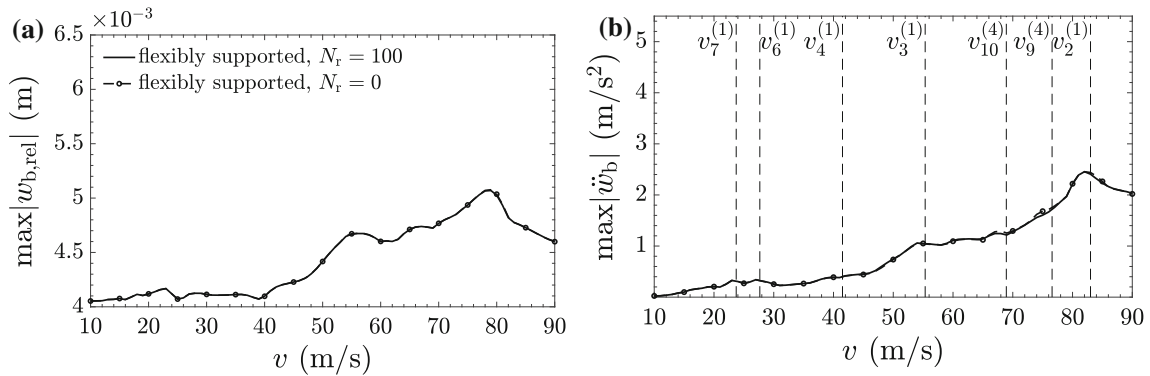
Fig. 10 a Maximum absolute bridge deflection, and **b** maximum absolute bridge acceleration for the flexibly supported bridge
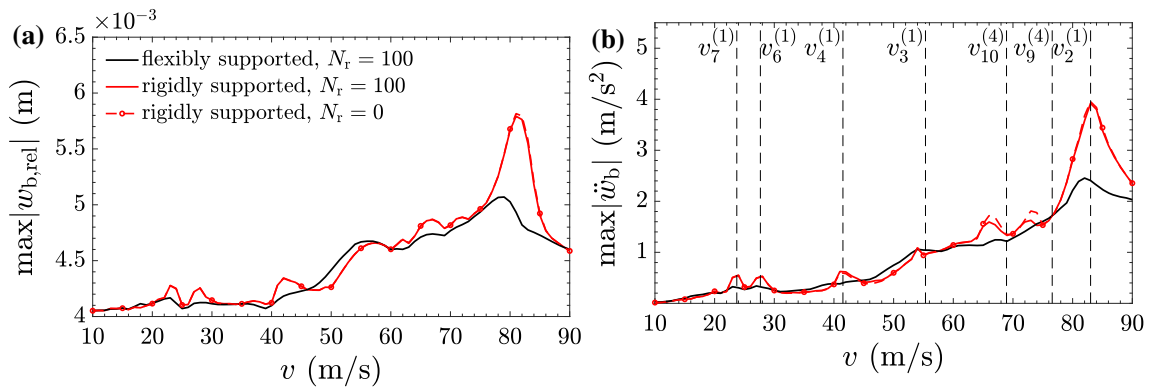

Fig. 11 a Maximum absolute bridge deflection, and **b** maximum absolute bridge acceleration for the flexibly and rigidly supported bridges

the resonance speed $v_2^{(1)}$ it is more than 60%. This result demonstrates how important it can be to include the properties of the subsoil when calculating the response, albeit often ignored in standard models. In addition, this Figure shows the response spectra of the simply supported bridge for $w_r^{(f)} = 0$ (i.e., $N_r = 0$). Here, it can be seen that for the maximum accelerations in the speed range between 65 and 76 m/s a slight overestimation occurs compared to the solution considering $w_r^{(f)}(N_r = 100)$.

Subsequently, the influence of the track on the predicted bridge response is investigated, which is also not considered in the common beam models. Figure 12 therefore shows, in addition to the results of the proposed model, the solution for the corresponding viscoelastically supported beam without track (referred to as "flexibly supported, no track"). In the latter model, following a recently introduced method [20], the load distribution shortly before and after the bridge is considered in a simplified manner by an approach and a departure phase of lengths L_a and L_d, respectively. Due to the very isolated deflection of the track around the axle loads, the lengths $L_a = L_d = 1$ m were used. For speeds $v > 30$ m/s, the deflection of the bridge based on the model without rail and the model presented here agree very well, as shown in Fig. 12a, while in the lower speed range the model without track subsystem overestimates this response quantity. However, the predicted peak accelerations shown in Fig. 12b depend strongly on the model approach in the entire speed range. The accelerations predicted with the proposed model are significantly lower than those of the model without rail. This behavior is explained by the improved description of the load distribution over the track subsystem as well as possible damping effects due to ballast damping. This result emphasizes the need to take the track subsystem into account when computing the bridge acceleration, but in many cases, this is usually not done. As an additional reference, the results of a rigidly supported bridge without track (referred to as "rigidly supported, no track") are included in Fig. 12, again showing the significantly higher acceleration response if the interaction with the underlying soil is neglected.

In this study assuming a perfectly straight and smooth track, no substantial influence of the number of considered rail modes (in $w_r^{(f)}$) on the bridge response was observed for the flexibly supported structure.
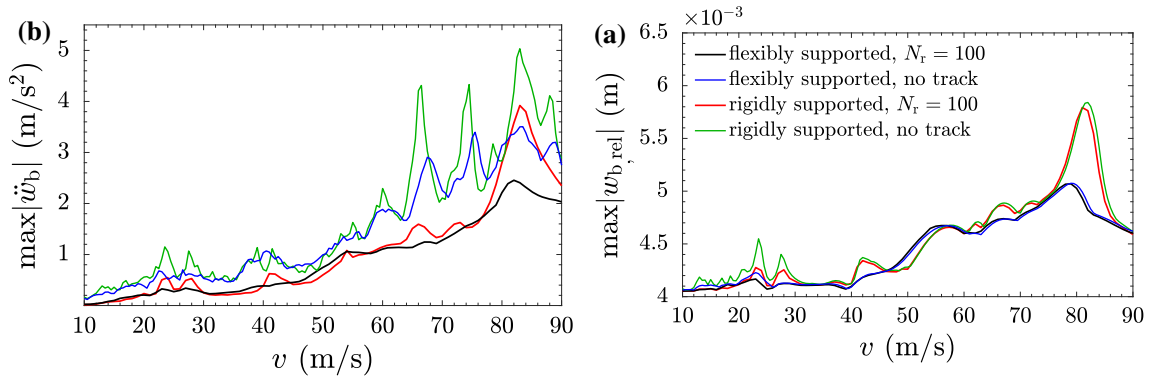
Fig. 12 a Maximum absolute bridge deflection, and **b** maximum absolute bridge acceleration for the flexibly and rigidly supported bridges, with and without the track
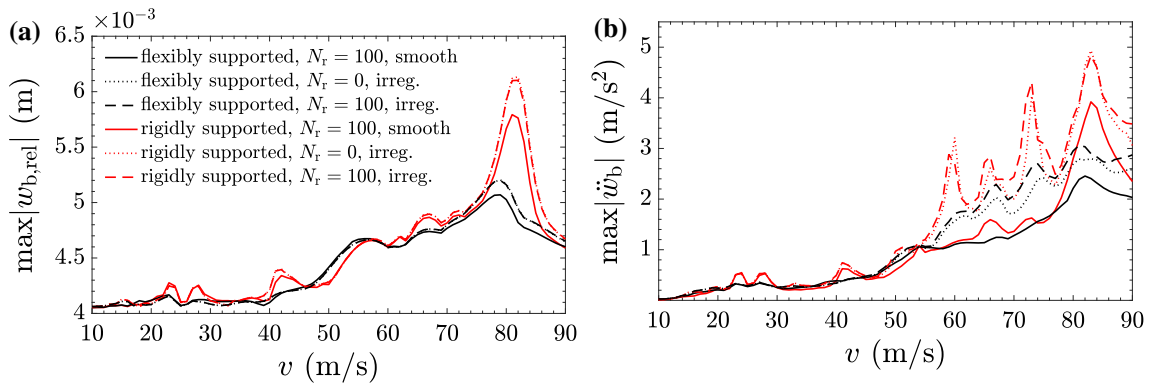

Fig. 13 a Maximum absolute bridge deflection, and **b** maximum absolute bridge acceleration, with and without track irregularities

To verify this behavior in the presence of track irregularities, the computations are repeated with $N_r = 0$ and $N_r = 100$ track modes, respectively, however, assigning the random rail irregularity profile I_{irr} for a moderate quality track shown in Fig. 7 to the track. Figure 13, which compares the bridge response for the system with and without track irregularity, shows now a larger effect of these modes on the bridge acceleration when irregularities of the track are considered. This effect is more pronounced in the case of the flexibly supported beam, since the maximum acceleration is underestimated by up to 16.7% when $w_r^{(f)}$ is neglected (i.e., $N_r = 0$), compared to the result based on $N_r = 100$. Further preliminary comparative calculations have shown that the magnitude of this deviation can be even much larger when other track parameters are used and rail irregularities of a poor quality track are considered. In contrast, the maximum deflection of the bridge remains largely unaffected by the number of rail modes considered, even in the case of track irregularities, as shown in Fig. 13a. From this study, it can be concluded that the dynamic track deflection $w_r^{(f)}$ has little effect on *bridge displacement*, but is more important for accurately predicting the *bridge acceleration* in the presence of rail irregularities.

7 Summary and conclusions

In this paper, a novel methodology for predicting the response of railway bridges subjected to high-speed trains was presented, based on component mode synthesis and a discrete substructuring technique. In the beam model of the bridge, both the soil under the foundations and the track are included in a simplified manner. The coupling of the plane mass–spring–damper model of the train and the non-classically damped soil–bridge–track interaction model is achieved with the so-called corresponding assumption. A major advantage of the proposed methodology is that the number of modes (and thus the number of degrees of freedom) of the tack and the soil–bridge subsystem included in the analysis can be chosen differently and adapted to the problem. A comparative calculation with a less efficient finite element model proved the accuracy of this approach. The

proposed approach allows to investigate effects like soil–structure interaction, bridge–track interaction as well as bridge–train interaction efficiently and with relatively low numerical effort.

An example bridge was used to show the influence of the subsoil, track, and track irregularities on the numerically predicted bridge response. From these results, the following preliminary conclusions can be drawn:

– The results support the well-known fact that dynamic bridge deflection is generally less sensitive to model detail than bridge acceleration
– Depending on its properties, the soil can have a significant impact on the predicted bridge response, in particular at higher speeds and resonance. Due to the radiation damping, over wide speed ranges the response of the model with soil is smaller than for the rigidly supported bridge model. At certain train speeds, however, an increase of the response can occur due to the frequency reduction and the occurrence of additional natural frequencies.
– Consideration of the track in the model leads to a reduction in the bridge acceleration due to the load-distributing effect and the damping of the track bed. In contrast, the bridge deflection is hardly influenced by the track model.
– The dynamic response of the track has little effect on the bridge response if the track is perfectly straight and smooth. However, if track irregularities are taken into account, the dynamics of the track can no longer be neglected when calculating the bridge acceleration, in particular in the higher speed range.

The general validity of these conclusions needs to be substantiated by further extensive parameter studies.

Declarations

Appendix A: Modal properties of the bridge–soil substructure

The eigenfunctions of the Euler–Bernoulli beam bridge substructure [9,43]

$$\Phi(x) = C_1 \sin \frac{\lambda x}{L} + C_2 \cos \frac{\lambda x}{L} + C_3 \sinh \frac{\lambda x}{L} + C_4 \cosh \frac{\lambda x}{L} \tag{54}$$

are adjusted to the boundary conditions (Eq. (12)). Since the beam is non-classically damped due to the spring–damper elements below the bearings, the infinite number of eigenvalues λ_b resulting from zeroing the coefficient determinant of the four corresponding equations appears in complex conjugate pairs, referred to as $\lambda_b^{(m)}$, $(m = 1, \ldots, \infty)$ and its conjugate complex counterpart as $\bar{\lambda}_b^{(m)}$. The mth complex natural frequency $s_b^{(m)}$ of the stand-alone beam, which is related to the mth eigenvalue $\lambda_b^{(m)}$ according to

$$\left(s_b^{(m)}\right)^2 = -\frac{\left(\lambda_b^{(m)}\right)^4}{L_b^4} \frac{E I_b}{\rho A_b} \tag{55}$$

is composed of a real and an imaginary part, $s_b^{(m)} = \sigma_b^{(m)} + i\Omega_b^{(m)}$ [4,29]. The corresponding conjugate complex frequency is denoted as $\bar{s}_b^{(m)} = \sigma_b^{(m)} - i\Omega_b^{(m)}$. The real part $\sigma_b^{(m)}$ of $s_b^{(m)}$ is referred to as decay rate and the imaginary part $\Omega_b^{(m)}$ as the damped mth natural frequency. The absolute value of $s_b^{(m)}$ is the so-called pseudo-undamped natural frequency of the bridge beam,

$$\omega_b^{(m)} = \left| s_b^{(m)} \right| = \sqrt{\left(\sigma_b^{(m)}\right)^2 + \left(\Omega_b^{(m)}\right)^2}, \tag{56}$$

and the ratio

$$\zeta_b^{(m)} = \frac{-\Re\left(s_b^{(m)}\right)}{\left| s_b^{(m)} \right|} = -\frac{\sigma_b^{(m)}}{\omega_b^{(m)}} \tag{57}$$

corresponds to the mth modal equivalent damping ratio [19] of the non-classically damped beam substructure. This equivalent damping coefficient takes into account the damping due to the dashpot dampers at the ends of the bridge. If the structural damping of the beam is also to be considered, this is simply done by adding the mth modal structural damping $\tilde{\zeta}_b^{(m)}$ coefficient to the mth modal equivalent damping coefficient $\zeta_b^{(m)}$, i.e., $\tilde{\zeta}_b^{(m)} + \zeta_b^{(m)}$ [20]. In this case, the mth complex natural frequency becomes [20]

$$s_b^{(m)} = -\omega_b^{(m)}\left(\zeta_b^{(m)} + \tilde{\zeta}_b^{(m)}\right) + i\omega_b^{(m)}\sqrt{1 - \left(\zeta_b^{(m)} + \tilde{\zeta}_b^{(m)}\right)^2}. \tag{58}$$

By inserting the unmodified eigenvalues $\lambda_b^{(m)}$ into Eq. (54), three of the constants $C_1^{(m)}, C_2^{(m)}, C_3^{(m)}, C_4^{(m)}$ of the mth eigenfunction $\Phi_b^{(m)}(x)$ can be expressed by the fourth. This constant can be scaled arbitrarily. The corresponding conjugate complex eigenfunction is denoted as $\bar{\Phi}_b^{(m)}(x)$.

The orthogonality relations of the eigenfunctions read as [15,20,24]

$$a_b^{(m)}\delta_{lm} = c_b \left(\Phi_b^{(m)}(0)\Phi_b^{(l)}(0) + \Phi_b^{(m)}(L_b)\Phi_b^{(l)}(L_b)\right)$$
$$+ \left(s_b^{(l)} + s_b^{(m)}\right)\left(\rho_b A_b \int_0^{L_b} \Phi_b^{(m)}(x)\Phi_b^{(l)}(x)dx\right.$$
$$+ \left.m_b\left(\Phi_b^{(m)}(0)\Phi_b^{(l)}(0) + \Phi_b^{(m)}(L_b)\Phi_b^{(l)}(L_b)\right)\right), \tag{59}$$

$$b_b^{(m)}\delta_{lm} = k_b\left(\Phi_b^{(m)}(0)\Phi_b^{(l)}(0) + \Phi_b^{(m)}(L_b)\Phi_b^{(l)}(L_b)\right) + EI_b\int_0^{L_b}\Phi_{b,xx}^{(m)}(x)\Phi_{b,xx}^{(l)}(x)dx$$
$$- \left(s_b^{(m)}s_b^{(l)}\right)\left(\rho_b A_b\int_0^{L_b}\Phi_b^{(m)}(x)\Phi_b^{(l)}(x)dx\right.$$
$$+ \left.m_b\left(\Phi_b^{(m)}(0)\Phi_b^{(l)}(0) + \Phi_b^{(m)}(L_b)\Phi_b^{(l)}(L_b)\right)\right). \tag{60}$$

The normalizing constants $a_b^{(m)} = 2s_b^{(m)}M_b^{(m)}$ and $b_b^{(m)} = -2\left(s_b^{(m)}\right)^2 M_b^{(m)}$ are both related to the generalized modal mass $M_b^{(m)}$, which can be expressed as

$$M_b^{(m)} = \frac{c_b}{2s_b^{(m)}}\left(\left(\Phi_b^{(m)}(0)\right)^2 + \left(\Phi_b^{(m)}(L_b)\right)^2\right)$$
$$+ \rho_b A_b\int_0^{L_b}\left(\Phi_b^{(m)}(x)\right)^2 dx + m_b\left(\left(\Phi_b^{(m)}(0)\right)^2 + \left(\Phi_b^{(m)}(L_b)\right)^2\right). \tag{61}$$

Appendix B: Modal properties of the track substructure

The eigenvalue problem of the track substructure beam model is derived from the homogeneous form of the equation of motion (Eq. (2)),

$$EI_r\Phi_{r,xxxx}(x) + \left(s_r^2\rho A_r + s_r c_f(x) + k_f(x)\right)\Phi_r(x) = 0, \tag{62}$$

and the relations $\dot{y}_r = s_r y_r$ and $\ddot{y}_r = s_r^2 y_r$ resulting from the general expression $y_r(t) = Ce^{(s_r t)}$ [20,28]. Conveniently, the natural frequencies of this substructure are found considering one half of the track model, because the piecewise differently bedded beam model is symmetric, and thus symmetry and antimetry of the eigenfunctions apply. For the analysis of eigenmodes, half the beam is first divided into the segment above the soil and the segment above the bridge. The local axial coordinate of the segment above the soil is denoted as $x_1 = x + L_0$ and has its origin at the left end of the track (Fig. 1, point (A)), whereas the axial coordinate for the section above the bridge denoted as $x_2 = x$ has its origin at the left viscoelastic bridge bearing (Fig. 1, point (B)). The eigenvalue problem now written separately for each beam segment,

$$EI_r\Phi_{r0,xxxx}(x_1) + \left(s_r^2\rho A_r + s_r c_{f0} + k_{f0}\right)\Phi_{r0}(x_1) = 0 \text{ for } 0 \leq x_1 \leq L_0, \tag{63}$$

$$EI_r\Phi_{rb,xxxx}(x_2) + \left(s_r^2\rho A_r + s_r c_{fb} + k_{fb}\right)\Phi_{rb}(x_2) = 0 \text{ for } 0 < x_2 \leq L_b/2, \tag{64}$$

yields the eigenmodes in the form of Eq. (54) [9,43],

$$\Phi_{r0}(x_1) = C_{r0(1)}\sin\frac{\lambda_{r0}x_1}{L_0} + C_{r0(2)}\cos\frac{\lambda_{r0}x_1}{L_0} + C_{r0(3)}\sinh\frac{\lambda_{r0}x_1}{L_0} + C_{r0(4)}\cosh\frac{\lambda_{r0}x_1}{L_0},$$

$$\Phi_{rb}(x_1) = C_{rb(1)}\sin\frac{\lambda_{rb}x_2}{L_b/2} + C_{rb(2)}\cos\frac{\lambda_{rb}x_2}{L_b/2} + C_{rb(3)}\sinh\frac{\lambda_{rb}x_2}{L_b/2} + C_{rb(4)}\cosh\frac{\lambda_{rb}x_2}{L_b/2}, \tag{65}$$

where

$$\lambda_{r0} = L_0\sqrt[4]{-\frac{s_r^2\rho A_r + s_r c_{r0} + k_{f0}}{EI_r}}, \quad \lambda_{rb} = \frac{L_b}{2}\sqrt[4]{-\frac{s_r^2\rho A_r + s_r c_{rb} + k_{fb}}{EI_r}}. \tag{66}$$

The eigenvalue λ_{r0} can be expressed in terms of the eigenvalue λ_{rb} by solving the equation for λ_{rb} in Eq. (66) for the eigenfrequency s_r,

$$s_r = \frac{1}{2\rho A_r}\left(-c_{fb} \pm \sqrt{c_{fb}^2 - 4k_{fb}\rho A_r - \frac{\lambda_{rb}^4 EI_r\rho A_r}{L_0^4}}\right), \tag{67}$$

and inserting this relation in the expression for λ_{r0}. Adjusting Eq. (65) to the boundary conditions at the left end of the beam,

$$\Phi_{r0}(x_1 = 0) = 0, \quad \Phi_{r0,xx}(x_1 = 0) = 0, \tag{68}$$

the continuity conditions between the beam segments,

$$\begin{array}{ll}
\Phi_{r0}(x_1 = L_0) = \Phi_{rb}(x_2 = 0), & \Phi_{r0,x}(x_1 = L_0) = \Phi_{rb,x}(x_2 = 0), \\
\Phi_{r0,xx}(x_1 = L_0) = \Phi_{rb,xx}(x_2 = 0), & \Phi_{r0,xxx}(x_1 = L_0) = \Phi_{rb,xxx}(x_2 = 0),
\end{array} \tag{69}$$

and the continuity conditions at the center of the track beam,

$$\begin{array}{lll}
\text{antimetry}: & \Phi_{rb}(x_2 = L_b/2) = 0, & \Phi_{rb,xx}(x_2 = L_b/2) = 0, \\
\text{symmetry}: & \Phi_{rb,x}(x_2 = L_b/2) = 0, & \Phi_{rb,xxx}(x_2 = L_b/2) = 0,
\end{array} \tag{70}$$

and zeroing the coefficient determinant of the four corresponding equations yields the eigenvalues $\lambda_{rb}^{(n)}$, ($n = 1, \ldots, \infty$) and their complex conjugate counterparts $\bar{\lambda}_{rb}^{(n)}$. The nth complex frequency can be expressed as $s_r^{(n)} = \sigma_r^{(n)} + i\Omega_r^{(n)}$ with the complex conjugate counterpart $\bar{s}_r^{(n)} = \sigma_r^{(n)} - i\Omega_r^{(n)}$. The pseudo-undamped natural frequency $\omega_r^{(n)}$ as well as the modal equivalent damping ratio $\zeta_r^{(n)}$ can be found in analogy to Eqs. (56)

and (57). Structural damping can be considered in analogy to Eq. (58) by adding the nth modal structural damping $\tilde{\zeta}_r^{(n)}$ to the nth equivalent damping coefficient $\zeta_r^{(n)}$,

$$s_r^{(n)} = -\omega_r^{(n)}\left(\zeta_r^{(n)} + \tilde{\zeta}_r^{(n)}\right) + i\omega_r^{(n)}\sqrt{1 - \left(\zeta_r^{(n)} + \tilde{\zeta}_r^{(n)}\right)^2}. \tag{71}$$

The resulting eigenvalues $\lambda_{rb}^{(n)}$ are inserted in the corresponding set of eight equations to express seven of the coefficients $C_{r0(1)}^{(n)}$, $C_{r0(2)}^{(n)}$, $C_{r0(3)}^{(n)}$, $C_{r0(4)}^{(n)}$, $C_{rb(1)}^{(n)}$, $C_{rb(2)}^{(n)}$, $C_{rb(3)}^{(n)}$, $C_{rb(4)}^{(n)}$ by the eighth, which can be scaled arbitrarily. Eventually, the eigenfunctions of the total track substructure composed of the sectional eigenfunctions of Eq. (65) read as

$$\Phi_r^{(n)}(x) = \begin{cases} \Phi_{r0}^{(n)}(x + L_0) & -L_0 \leq x \leq 0 \\ \Phi_{rb}^{(n)}(x) & 0 < x \leq L_b/2 \\ \Phi_{rb}^{(n)}(L_b - x) & L_b/2 < x \leq L_b \\ \Phi_{r0}^{(n)}(L_b + L_0 - x) & L_b < x \leq L_b + L_0 \\ -\Phi_{rb}^{(n)}(L_b - x) & L_b/2 < x \leq L_b \\ -\Phi_{r0}^{(n)}(L_b + L_0 - x) & L_b < x \leq L_b + L_0 \end{cases} \left.\begin{matrix} \\ \\ \end{matrix}\right\} \begin{matrix} \text{symmetric} \\ (n = 1, 3, 5, \ldots) \\ \text{antimetric} \\ (n = 2, 4, 6, \ldots) \end{matrix} , \tag{72}$$

For the corresponding complex conjugate $\bar{\Phi}_r^{(n)}(x)$ the same relations apply.

The orthogonality relations can be derived as [15,20,24]

$$a_r^{(n)}\delta_{mn} = \int_{-L_0}^{L_b+L_0} c_f(x)\Phi_r^{(n)}(x)\Phi_r^{(m)}(x)dx$$
$$+ \left(s_r^{(m)} + s_r^{(n)}\right)\rho A_r \int_{-L_0}^{L_b+L_0} \Phi_r^{(n)}(x)\Phi_r^{(m)}(x)dx, \tag{73}$$

$$b_r^{(n)}\delta_{mn} = \int_{-L_0}^{L_b+L_0} k_f(x)\Phi_r^{(n)}(x)\Phi_r^{(m)}(x)dx$$
$$+ EI_r \int_{-L_0}^{L_b+L_0} \Phi_{r,xx}^{(n)}(x)\Phi_{r,xx}^{(m)}(x)dx$$
$$- \left(s_r^{(n)}s_r^{(m)}\right)\rho A_r \int_{-L_0}^{L_b+L_0} \Phi_r^{(n)}(x)\Phi_r^{(m)}(x)dx \tag{74}$$

with $a_r^{(n)} = 2s_r^{(n)}M_r^{(n)}$ and $b_r^{(n)} = -2\left(s_r^{(n)}\right)^2 M_r^{(n)}$ related to modal mass $M_r^{(n)}$,

$$M_r^{(n)} = \frac{1}{2s_r^{(n)}}\int_{-L_0}^{L_r+L_0} c_f(x)\left(\Phi_r^{(n)}(x)\right)^2 dx + \rho A_r \int_{-L_0}^{L_r+L_0}\left(\Phi_r^{(n)}(x)\right)^2 dx, \tag{75}$$

Appendix C: Substructure consolidation

Given that $\dot{\Phi}_r^{(n)}(x = x_k^{(j)}(t)) = \frac{d\Phi_r^{(n)}}{dt} = \frac{\partial \Phi_r^{(n)}}{\partial x}\frac{\partial x_k^{(j)}}{\partial t} = v\Phi_{r,x}^{(n)}(x_k^{(j)})$ and $\dot{\Psi}_r^{(n)}(x = x_k^{(j)}(t)) = \frac{d\Psi_r^{(n)}}{dt} = \frac{\partial \Psi_r^{(n)}}{\partial x}\frac{\partial x_k^{(j)}}{\partial t} = v\Psi_{r,x}^{(n)}(x_k^{(j)})$, the velocity and acceleration of the wheel at position $x_k^{(j)}(t)$ are expressed as

$$
\begin{aligned}
\dot{u}_{ak}^{(j)}(x_k^{(j)}) = \dot{w}_r\left(x_k^{(j)}, t\right) + \dot{I}_{irr}\left(x_k^{(j)}\right) &\approx \sum_{n=1}^{N_r}\left(v\Phi_{r,x}^{(n)}\left(x_k^{(j)}\right)y_r^{(n)}(t) + \Phi_r^{(n)}\left(x_k^{(j)}\right)\dot{y}_r^{(n)}(t)\right) \\
&+ \sum_{n=1}^{N_r}\left(v\bar{\Phi}_{r,x}^{(n)}\left(x_k^{(j)}\right)\bar{y}_r^{(n)}(t) + \bar{\Phi}_r^{(n)}\left(x_k^{(j)}\right)\dot{\bar{y}}_r^{(n)}(t)\right) \\
&+ \sum_{m=1}^{N_b}\left(v\Psi_{r,x}^{(m)}\left(x_k^{(j)}\right)y_b^{(m)}(t) + \Psi_r^{(m)}\left(x_k^{(j)}\right)\dot{y}_b^{(m)}(t)\right) \\
&+ \sum_{m=1}^{N_b}\left(v\bar{\Psi}_{r,x}^{(m)}\left(x_k^{(j)}\right)\bar{y}_b^{(m)}(t) + \bar{\Psi}_r^{(m)}(x_k^{(j)})\dot{\bar{y}}_b^{(m)}(t)\right) + \dot{I}_{irr}(x_k^{(j)})
\end{aligned} \tag{76}
$$

and

$$
\begin{aligned}
\ddot{u}_{ak}^{(j)}\left(x_k^{(j)}\right) = \ddot{w}_r\left(x_k^{(j)}, t\right) + \ddot{I}_{irr}\left(x_k^{(j)}\right) & \\
\approx \sum_{n=1}^{N_r}&\left(v^2\Phi_{r,xx}^{(n)}\left(x_k^{(j)}\right)y_r^{(n)}(t) + 2v\Phi_{r,x}^{(n)}(x_k^{(j)})\dot{y}_r^{(n)}(t) + \Phi_r^{(n)}(x_k^{(j)})\ddot{y}_r^{(n)}(t)\right) \\
+ \sum_{n=1}^{N_r}&\left(v^2\bar{\Phi}_{r,xx}^{(n)}\left(x_k^{(j)}\right)\bar{y}_r^{(n)}(t) + 2v\bar{\Phi}_{r,x}^{(n)}\left(x_k^{(j)}\right)\dot{\bar{y}}_r^{(n)}(t) + \bar{\Phi}_r^{(n)}\left(x_k^{(j)}\right)\ddot{\bar{y}}_r^{(n)}(t)\right) \\
+ \sum_{m=1}^{N_b}&\left(v^2\Psi_{r,xx}^{(m)}\left(x_k^{(j)}\right)y_b^{(m)}(t) + 2v\Psi_{r,x}^{(m)}\left(x_k^{(j)}\right)\dot{y}_b^{(m)}(t) + \Psi_r^{(m)}(x_k^{(j)})\ddot{y}_b^{(m)}(t)\right) \\
+ \sum_{m=1}^{N_b}&\left(v^2\bar{\Psi}_{r,xx}^{(m)}\left(x_k^{(j)}\right)\bar{y}_b^{(m)}(t) + 2v\bar{\Psi}_{r,x}^{(m)}\left(x_k^{(j)}\right)\dot{\bar{y}}_b^{(m)}(t) + \bar{\Psi}_r^{(m)}\left(x_k^{(j)}\right)\ddot{\bar{y}}_b^{(m)}(t)\right) + \ddot{I}_{irr}\left(x_k^{(j)}\right).
\end{aligned} \tag{77}
$$

The time-dependent transformation matrices $\mathbf{\Gamma}_1(t)$ and $\mathbf{\Gamma}_2(t)$ in Eq. (48) read as

$$
\mathbf{\Gamma}_1(t) = \begin{bmatrix}
\mathbf{I}_b & \mathbf{0} & \mathbf{0} & \mathbf{0} & \dots & \mathbf{0} & \mathbf{0} & \mathbf{0} & \dots & \mathbf{0} \\
\mathbf{0} & \mathbf{I}_r & \mathbf{0} & \mathbf{0} & \dots & \mathbf{0} & \mathbf{0} & \mathbf{0} & \dots & \mathbf{0} \\
\mathbf{D}_{\Psi_r}^{(1)} & \mathbf{D}_{\Phi_r}^{(1)} & \mathbf{J}_c & \mathbf{0} & \dots & \mathbf{0} & \mathbf{0} & \mathbf{0} & \dots & \mathbf{0} \\
\mathbf{D}_{\Psi_r}^{(2)} & \mathbf{D}_{\Phi_r}^{(2)} & \mathbf{0} & \mathbf{J}_c & \dots & \mathbf{0} & \mathbf{0} & \mathbf{0} & \dots & \mathbf{0} \\
\vdots & \vdots & \vdots & \vdots & \ddots & \vdots & \vdots & \vdots & \ddots & \vdots \\
\mathbf{D}_{\Psi_r}^{(N_c)} & \mathbf{D}_{\Phi_r}^{(N_c)} & \mathbf{0} & \mathbf{0} & \dots & \mathbf{J}_c & \mathbf{0} & \mathbf{0} & \dots & \mathbf{0} \\
\dot{\mathbf{D}}_{\Psi_r}^{(1)} & \dot{\mathbf{D}}_{\Phi_r}^{(1)} & \mathbf{0} & \mathbf{0} & \dots & \mathbf{0} & \mathbf{J}_c & \mathbf{0} & \dots & \mathbf{0} \\
\dot{\mathbf{D}}_{\Psi_r}^{(2)} & \dot{\mathbf{D}}_{\Phi_r}^{(2)} & \mathbf{0} & \mathbf{0} & \dots & \mathbf{0} & \mathbf{0} & \mathbf{J}_c & \dots & \mathbf{0} \\
\vdots & \vdots & \vdots & \vdots & \ddots & \vdots & \vdots & \vdots & \ddots & \vdots \\
\dot{\mathbf{D}}_{\Psi_r}^{(N_c)} & \dot{\mathbf{D}}_{\Phi_r}^{(N_c)} & \mathbf{0} & \mathbf{0} & \dots & \mathbf{0} & \mathbf{0} & \mathbf{0} & \dots & \mathbf{J}_c
\end{bmatrix}, \tag{78}
$$

$$\boldsymbol{\Gamma}_2(t) = \begin{bmatrix} \mathbf{0} & \mathbf{0} & 0 & 0 & \dots & 0 & 0 & 0 & \dots & 0 \\ \mathbf{0} & \mathbf{0} & 0 & 0 & \dots & 0 & 0 & 0 & \dots & 0 \\ \mathbf{0} & \mathbf{0} & 0 & 0 & \dots & 0 & 0 & 0 & \dots & 0 \\ \mathbf{0} & \mathbf{0} & 0 & 0 & \dots & 0 & 0 & 0 & \dots & 0 \\ \vdots & \vdots & \vdots & \vdots & \ddots & \vdots & \vdots & \vdots & \ddots & \vdots \\ \mathbf{0} & \mathbf{0} & 0 & 0 & \dots & 0 & 0 & 0 & \dots & 0 \\ \mathbf{D}_{\boldsymbol{\Psi}_{\mathrm{r}}}^{(1)} & \mathbf{D}_{\boldsymbol{\Phi}_{\mathrm{r}}}^{(1)} & 0 & 0 & \dots & 0 & 0 & 0 & \dots & 0 \\ \mathbf{D}_{\boldsymbol{\Psi}_{\mathrm{r}}}^{(2)} & \mathbf{D}_{\boldsymbol{\Phi}_{\mathrm{r}}}^{(2)} & 0 & 0 & \dots & 0 & 0 & 0 & \dots & 0 \\ \vdots & \vdots & \vdots & \vdots & \dots & \vdots & \vdots & \vdots & \ddots & \vdots \\ \mathbf{D}_{\boldsymbol{\Psi}_{\mathrm{r}}}^{(N_{\mathrm{c}})} & \mathbf{D}_{\boldsymbol{\Phi}_{\mathrm{r}}}^{(N_{\mathrm{c}})} & 0 & 0 & \dots & 0 & 0 & 0 & \dots & 0 \end{bmatrix} \tag{79}$$

with $\mathbf{I}_{\mathrm{b}}$ being an identity matrix of dimension $[2N_{\mathrm{b}} \times 2N_{\mathrm{b}}]$ and $\mathbf{I}_{\mathrm{r}}$ the identity matrix of dimension $[2N_{\mathrm{r}} \times 2N_{\mathrm{r}}]$. The matrix

$$\mathbf{J}_{\mathrm{c}} = \begin{bmatrix} \mathbf{I}_{\mathrm{c}}^{[6 \times 6]} \\ \mathbf{0}^{[4 \times 6]} \end{bmatrix} \tag{80}$$

indicates the DOFs of the vehicle body and bogies of the jth vehicle by including the identity matrix $\mathbf{I}_{\mathrm{c}}$ and setting the remaining rows, corresponding to the DOFs of the four axles, to zero. The sub-matrices

$$\mathbf{D}_{\boldsymbol{\Psi}_{\mathrm{r}}}^{(j)}(t) = \begin{bmatrix} \mathbf{0}^{[6 \times 2N_{\mathrm{b}}]} \\ \boldsymbol{\Pi}^{(j)}(t)\boldsymbol{\Psi}_{\mathrm{r}}^{(j)\mathrm{T}}(t) \end{bmatrix}, \quad \mathbf{D}_{\boldsymbol{\Phi}_{\mathrm{r}}}^{(j)}(t) = \begin{bmatrix} \mathbf{0}^{[6 \times 2N_{\mathrm{r}}]} \\ \boldsymbol{\Pi}^{(j)}(t)\boldsymbol{\Phi}_{\mathrm{r}}^{(j)\mathrm{T}}(t) \end{bmatrix} \tag{81}$$

are composed of the shape functions and eigenfunctions of the track evaluated at the axle positions $x_k^{(j)}(t)$ with $\boldsymbol{\Pi}^{(j)}(t)$ as the previously defined window function only allowing the displacements of axles between beginning and end of the track to be non-zero. The vector

$$\boldsymbol{\Upsilon}(t) = \left[\mathbf{0}, \mathbf{I}_{\mathrm{irr}}^{(1)}(t), \mathbf{I}_{\mathrm{irr}}^{(2)}(t), \dots, \mathbf{I}_{\mathrm{irr}}^{(N_{\mathrm{c}})}(t)\right]^{\mathrm{T}} \tag{82}$$

with

$$\mathbf{I}_{\mathrm{irr}}^{(j)}(t) = \begin{bmatrix} \mathbf{0}^{[6 \times 1]} \\ \Pi\left(t, t_{\mathrm{A1}}^{(j)}, t_{\mathrm{D1}}^{(j)}\right) I_{\mathrm{irr}}\left(x_1^{(j)}(t)\right) \\ \Pi\left(t, t_{\mathrm{A2}}^{(j)}, t_{\mathrm{D2}}^{(j)}\right) I_{\mathrm{irr}}\left(x_2^{(j)}(t)\right) \\ \Pi\left(t, t_{\mathrm{A3}}^{(j)}, t_{\mathrm{D3}}^{(j)}\right) I_{\mathrm{irr}}\left(x_3^{(j)}(t)\right) \\ \Pi\left(t, t_{\mathrm{A4}}^{(j)}, t_{\mathrm{D4}}^{(j)}\right) I_{\mathrm{irr}}\left(x_4^{(j)}(t)\right) \end{bmatrix} \tag{83}$$

is the jth sub-vector containing the irregularity profiles at the four axle positions of the jth vehicle. The vector $\mathbf{0}$ in (82) has $2N_{\mathrm{b}} + 2N_{\mathrm{r}}$ entries, representing the DOFs of the bridge and track.

References

1. ABAQUS (2016).: Providence, RI, United States (2015)
2. Biondi, B., Muscolino, G.: Component-mode synthesis method for coupled continuous and FE discretized substructures. Eng. Struct. **25**(4), 419–433 (2003). https://doi.org/10.1016/S0141-0296(02)00183-9
3. Biondi, B., Muscolino, G., Sofi, A.: A substructure approach for the dynamic analysis of train-track-bridge system. Comput. Struct. **83**(28–30), 2271–2281 (2005). https://doi.org/10.1016/j.compstruc.2005.03.036
4. Brandt, A.: Noise and Vibration Analysis: Signal Analysis and Experimental Procedures/Anders Brandt. Wiley-Blackwell, Oxford (2011)
5. Bucinskas, P., Andersen, L.: Dynamic response of vehicle-bridge-soil system using lumped-parameter models for structure-soil interaction. Comput. Struct. **238**, 106270 (2020). https://doi.org/10.1016/j.compstruc.2020.106270
6. Butcher, J.C.: Numerical Methods for Ordinary Differential Equations, 3rd Edn. Wiley, Hoboken, New Jersey (2016)
7. Cheng, Y.S., Au, F.T.K., Cheung, Y.K.: Vibration of railway bridges under a moving train by using bridge-track-vehicle element. Eng. Struct. **23**(12), 1597–1606 (2001). https://doi.org/10.1016/S0141-0296(01)00058-X
8. Claus, H., Schiehlen, W.: Modeling and simulation of railway bogie structural vibrations. Veh. Syst. Dyn. **29**(sup1), 538–552 (1998). https://doi.org/10.1080/00423119808969585

9. Clough, R.W., Penzien, J.: Dynamics of Structures. McGraw-Hill, New York (1993)
10. Cojocaru, E.C., Irschik, H., Gattringer, H.: Dynamic response of an elastic bridge due to a moving elastic beam. Comput. Struct. **82**(11), 931–943 (2004). https://doi.org/10.1016/j.compstruc.2004.02.001
11. Das, B.M., Luo, Z.: Principles of Soil Dynamics. Cengage Learning (2016)
12. Den Hartog, J.P.: Advanced strength of materials. Dover Books on Engineering. Dover Publications, New York (1987)
13. Di Lorenzo, S., Di Paola, M., Failla, G., Pirrotta, A.: On the moving load problem in Euler-Bernoulli uniform beams with viscoelastic supports and joints. Acta Mech. **228**(3), 805–821 (2017). https://doi.org/10.1007/s00707-016-1739-6
14. Dimitrovová, Z.: New semi-analytical solution for a uniformly moving mass on a beam on a two-parameter visco-elastic foundation. Int. J. Mech. Sci. **127**, 142–162 (2017). https://doi.org/10.1016/j.ijmecsci.2016.08.025
15. Foss, K.A.: Coordinates which uncouple the equations of motion of damped linear dynamic systems. J. Appl. Mech. **25**, 361–364 (1958)
16. Frýba, L.: Dynamics of railway bridges. Thomas Telford Publishing (1996). https://doi.org/10.1680/dorb.34716
17. Frýba, L.: Vibration of Solids and Structures Under Moving Loads. Springer (1999). https://doi.org/10.1007/978-94-011-9685-7
18. Galvín, P., Domínguez, J.: High-speed train-induced ground motion and interaction with structures. J. Sound Vib. **307**(3), 755–777 (2007). https://doi.org/10.1016/j.jsv.2007.07.017
19. Genta, G.: Vibration Dynamics and Control. Mechanical Engineering Series. Springer, New York (2009)
20. Hirzinger, B., Adam, C., Salcher, P.: Dynamic response of a non-classically damped beam with general boundary conditions subjected to a moving mass-spring-damper system. Int. J. Mech. Sci. **185**, 105877 (2020). https://doi.org/10.1016/j.ijmecsci.2020.105877
21. Hirzinger, B., Adam, C., Salcher, P., Oberguggenberger, M.: On the optimal strategy of stochastic-based reliability assessment of railway bridges for high-speed trains. Meccanica **54**(9), 1385–1402 (2019). https://doi.org/10.1007/s11012-019-00999-0
22. Johansson, C., Nualláin, N.Á.N., Pacoste, C., Andersson, A.: A methodology for the preliminary assessment of existing railway bridges for high-speed traffic. Eng. Struct. **58**, 25–35 (2014). https://doi.org/10.1016/j.engstruct.2013.10.011
23. Knothe, K.: Rail Vehicle Dynamics. Springer, Cham, Switzerland (2016)
24. Krenk, S.: Complex modes and frequencies in damped structural vibrations. J. Sound Vib. **270**(4–5), 981–996 (2004). https://doi.org/10.1016/S0022-460X(03)00768-5
25. MATLAB (R2020a). Natick, Massachusetts (2020)
26. Nguyen, K., Goicolea, J.M., Galbadón, F.: Comparison of dynamic effects of high-speed traffic load on ballasted track using a simplified two-dimensional and full three-dimensional model. Proc. Inst. Mech. Eng. Part F: J. Rail Rapid Transit. **228**(2), 128–142 (2014). https://doi.org/10.1177/0954409712465710
27. Popp, K., Schiehlen, W.O., Kröger, M., Panning, L.: Ground Vehicle Dynamics. Springer, Berlin (2010)
28. Pradlwarter, H.: Personal Communication (2018)
29. Prater, G., Singh, R.: Eigenproblem formulation, solution and interpretation for non-proportionally damped continuous beams. J. Sound Vib. **143**(1), 125–142 (1990). https://doi.org/10.1016/0022-460X(90)90572-H
30. Romero, A., Solís, M., Domínguez, J., Galvín, P.: Soil-structure interaction in resonant railway bridges. Soil Dyn. Earthq. Eng. **47**, 108–116 (2013). https://doi.org/10.1016/j.soildyn.2012.07.014
31. Salcher, P., Adam, C.: Modeling of dynamic train-bridge interaction in high-speed railways. Acta Mech. **226**(8), 2473–2495 (2015). https://doi.org/10.1007/s00707-015-1314-6
32. Stokes, G.G.: Discussion of a Differential Equation Relating to the Breaking of Railway Bridges. Printed at the Pitt Press by John W. Parker (1849). https://doi.org/10.1017/CBO9780511702259.013
33. Stoura, C.D., Dimitrakopoulos, E.G.: A Modified Bridge System method to characterize and decouple vehicle–bridge interaction. Acta Mech. 1619–6937 (2020). https://doi.org/10.1007/s00707-020-02699-3
34. Stoura, C.D., Dimitrakopoulos, E.G.: Additional damping effect on bridges because of vehicle-bridge interaction. J. Sound Vib. **476**, 115294 (2020). https://doi.org/10.1016/j.jsv.2020.115294
35. Svedholm, C., Pacoste, C., Karoumi, R.: Modal properties of simply supported railway bridges due to soil-structure interaction. In: M. Papadrakakis, V. Papadopoulos, V. Plevris (eds.) COMPDYN, pp. 1709–1719 (2015)
36. Svedholm, C., Zangeneh, A., Pacoste, C., François, S., Karoumi, R.: Vibration of damped uniform beams with general end conditions under moving loads. Eng. Struct. **126**, 40–52 (2016). https://doi.org/10.1016/j.engstruct.2016.07.037
37. Ülker-Kaustell, M., Karoumi, R., Pacoste, C.: Simplified analysis of the dynamic soil-structure interaction of a portal frame railway bridge. Eng. Struct. **32**(11), 3692–3698 (2010). https://doi.org/10.1016/j.engstruct.2010.08.013
38. Willis, R.: Preliminary essay to the Appendix B: Experiment for determining the effects produced by causing weights to travel over bars with different velocities. Report of the commissions appointed to inquire into the application of iron to railway structures. W. Clowes and Sons (1849)
39. Wolf, J.P., Deeks, A.: Foundation Vibration Analysis: A Strength of Materials Approach. Butterworth-Heinemann, Oxford (2004)
40. Wu, Y.S., Yang, Y.B., Yau, J.D.: Three-dimensional analysis of train-rail-bridge interaction problems. Veh. Syst. Dyn. **36**, 1–35 (2001). https://doi.org/10.1076/vesd.36.1.1.3567
41. Yang, Y.B., Yau, J.D., Wu, Y.S.: Vehicle–Bridge Interaction Dynamics. With Applications to High-Speed Railways. World Scientific (2004). https://doi.org/10.1142/5541
42. Zangeneh, A., Svedholm, C., Andersson, A., Pacoste, C., Karoumi, R.: Identification of soil-structure interaction effect in a portal frame railway bridge through full-scale dynamic testing. Eng. Struct. **159**, 299–309 (2018). https://doi.org/10.1016/j.engstruct.2018.01.014
43. Zarek, J.H.B., Gibbs, B.M.: The derivation of eigenvalues and mode shapes for the bending motion of a damped beam with general end conditions. J. Sound Vib. **78**(2), 185–196 (1981). https://doi.org/10.1016/S0022-460X(81)80032-6
44. Zhai, W., Han, Z., Chen, Z., Ling, L., Zhu, S.: Train-track-bridge dynamic interaction: a state-of-the-art review. Veh. Syst. Dyn. **57**(7), 984–1027 (2019). https://doi.org/10.1080/00423114.2019.1605085

45. Zhang, N., Xia, H., Guo, W.W., De Roeck, G.: A vehicle-bridge linear interaction model and its validation. Int. J. Struct. Stab. Dyn. **10**(02), 335–361 (2010). https://doi.org/10.1142/S0219455410003464
46. Zhu, Z., Gong, W., Wang, L., Li, Q., Bai, Y., Yu, Z., Harik, I.E.: An efficient multi-time-step method for train-track-bridge interaction. Comput. Struct. **238**, 106270 (2017). https://doi.org/10.1016/j.compstruc.2017.11.004

Publisher's Note Springer Nature remains neutral with regard to jurisdictional claims in published maps and institutional affiliations.